










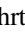
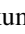






# Updated Planetary Mass Constraints of the Young V1298 Tau System Using MAROON-X

James Sikora<sup>1,2</sup> , Jason Rowe<sup>2</sup> , Saugata Barat<sup>1</sup>, Jacob L. Bean<sup>3</sup> , Madison Brady<sup>3</sup> , Jean-Michel Désert<sup>1</sup> , Adina D. Feinstein<sup>3,11</sup> , Emily A. Gilbert<sup>4</sup> , Gregory Henry<sup>5</sup> , David Kasper<sup>3</sup> , Déreck-Alexandre Lizotte<sup>2</sup>, Michael R. B. Matesic<sup>2,6,7</sup> , Vatsal Panwar<sup>1,8</sup> , Andreas Seifahrt<sup>3</sup> , Hinna Shivkumar<sup>1</sup> , Gudmundur Stefánsson<sup>9,12</sup> , and Julian Stürmer<sup>10</sup> 

<sup>1</sup> Anton Pannekoek Institute for Astronomy, University of Amsterdam, 1098 XH Amsterdam, The Netherlands; [james.t.sikora@gmail.com](mailto:james.t.sikora@gmail.com)

<sup>2</sup> Department of Physics & Astronomy, Bishop's University, 2600 Rue College, Sherbrooke, QC J1M 1Z7, Canada

<sup>3</sup> Department of Astronomy & Astrophysics, University of Chicago, Chicago, IL 60637, USA

<sup>4</sup> Jet Propulsion Laboratory, California Institute of Technology, 4800 Oak Grove Drive, Pasadena, CA 91109, USA

<sup>5</sup> Center of Excellence in Information Systems, Tennessee State University, Nashville, TN 37209, USA

<sup>6</sup> Département de Physique, Université de Montréal, 2900 Bd Édouard-Montpetit, Montréal, QC H3T 1J4, Canada

<sup>7</sup> Trottier Institute for Research on Exoplanets, Département de Physique, Université de Montréal, 2900 Bd Édouard-Montpetit, Montréal, QC H3T 1J4, Canada

<sup>8</sup> Department of Physics, University of Warwick, Coventry, West Midlands CV4 7AL, UK

<sup>9</sup> Department of Astrophysical Sciences, Princeton University, 4 Ivy Lane, Princeton, NJ 08540, USA

<sup>10</sup> Landessternwarte, Zentrum für Astronomie der Universität Heidelberg, Königstuhl 12, D-69117 Heidelberg, Germany

Received 2022 December 24; revised 2023 March 20; accepted 2023 March 27; published 2023 May 24

## Abstract

The early K-type T-Tauri star, V1298 Tau ( $V = 10$  mag, age  $\approx 20$ – $30$  Myr) hosts four transiting planets with radii ranging from  $4.9$  to  $9.6 R_{\oplus}$ . The three inner planets have orbital periods of  $\approx 8$ – $24$  days while the outer planet's period is poorly constrained by single transits observed with K2 and the Transiting Exoplanet Survey Satellite (TESS). Planets b, c, and d are proto-sub-Neptunes that may be undergoing significant mass loss. Depending on the stellar activity and planet masses, they are expected to evolve into super-Earths/sub-Neptunes that bound the radius valley. Here we present results of a joint transit and radial velocity (RV) modeling analysis, which includes recently obtained TESS photometry and MAROON-X RV measurements. Assuming circular orbits, we obtain a low-significance ( $\approx 2\sigma$ ) RV detection of planet c, implying a mass of  $19.8^{+9.3}_{-8.9} M_{\oplus}$  and a conservative  $2\sigma$  upper limit of  $< 39 M_{\oplus}$ . For planets b and d, we derive  $2\sigma$  upper limits of  $M_b < 159 M_{\oplus}$  and  $M_d < 41 M_{\oplus}$ , respectively. For planet e, plausible discrete periods of  $P_e > 55.4$  days are ruled out at the  $3\sigma$  level while seven solutions with  $43.3 < P_e/d < 55.4$  are consistent with the most probable  $46.768131 \pm 000076$  days solution within  $3\sigma$ . Adopting the most probable solution yields a  $2.6\sigma$  RV detection with a mass of  $0.66 \pm 0.26 M_{\text{Jup}}$ . Comparing the updated mass and radius constraints with planetary evolution and interior structure models shows that planets b, d, and e are consistent with predictions for young gas-rich planets and that planet c is consistent with having a water-rich core with a substantial ( $\sim 5\%$  by mass)  $\text{H}_2$  envelope.

*Unified Astronomy Thesaurus concepts:* Exoplanet astronomy (486); Exoplanets (498); Mini Neptunes (1063); Transits (1711); Radial velocity (1332); Exoplanet systems (484)

## 1. Introduction

Planets orbiting young stars ( $\lesssim 100$  Myr) serve as important windows into the early stages of planet formation and evolution. When coupled with known ages and insolation fluxes, bulk-density measurements of young planets can be used to infer the core compositions and masses of their primordial H/He-dominated atmospheres (Fortney et al. 2007; Lopez & Fortney 2014). Additionally, precise mass constraints of such planets provide a unique opportunity to test, inform, and constrain initial planet formation location theories (Lee & Chiang 2015, 2016; Owen 2020) and theories of atmospheric mass-loss processes (Kulow et al. 2014; Oklopčić & Hirata 2018). Transiting young planets are notoriously challenging to detect given the dominating underlying stellar variability of young stars. From the primary Kepler mission (Borucki et al. 2010), it was uncovered that young

planets are relatively rare ( $\lesssim 4\%$  of transiting planets discovered have ages  $< 1$  Gyr; Berger et al. 2020). Since the launch of the Transiting Exoplanet Survey Satellite (TESS; Ricker et al. 2014), fewer than a dozen young planets have been detected and confirmed (e.g., Benatti et al. 2019; Newton et al. 2019; Rizzuto et al. 2020; Carleo et al. 2021). Therefore, it is crucial that attempts be made to characterize these planets fully, particularly when they orbit bright, nearby host stars.

David et al. (2019a, 2019b) reported the detection of three transiting planets and one candidate planet orbiting the young ( $\approx 20$  Myr), bright ( $V = 10$  mag) T-Tauri star, V1298 Tau, which was observed during K2 Campaign 4 in 2016 (Howell et al. 2014). The planets have short orbital periods ( $\approx 8$ – $60$  days) and radii between that of Neptune and Jupiter, implying that they currently host substantial H/He-dominated atmospheres that could be substantially stripped as they evolve (Poppenhaeger et al. 2020). Additional transits were observed in 2021 with TESS (Feinstein et al. 2022) including a second transit of planet e, which was only previously observed once by K2. Recent mass constraints inferred from radial velocity (RV) measurements were published by Suárez Mascareño et al. (2021); these measurements estimated that planets b and e exhibit masses of  $\approx 0.6 M_{\text{Jup}}$  and  $1.2 M_{\text{Jup}}$ , respectively, and

<sup>11</sup> NSF Graduate Research Fellow.

<sup>12</sup> NASA Sagan Fellow.



that planets c and d have masses  $\lesssim 0.3 M_{\text{Jup}}$ . The reported mass of planet e is particularly surprising since it suggests that Jupiter-mass planets may contract much more rapidly than is predicted by planetary evolution models (Fortney et al. 2007; Baraffe et al. 2008). However, the 40.2 days period of planet e inferred by this study is incompatible with the timing of the K2 and TESS transits (Feinstein et al. 2022), which suggests that the mass constraint needs to be revised.

Young systems such as V1298 Tau are particularly challenging targets—both for transit and RV studies—due to the high degree of stellar activity exhibited by their host stars (Ibañez Bustos et al. 2019; Gilbert et al. 2022). Nonetheless, previous RV studies have demonstrated the feasibility of detecting and characterizing these planetary RV signatures with the aid of Gaussian Processes (GPs; Cloutier et al. 2019; Plavchan et al. 2020; Cale et al. 2021; Klein et al. 2021). In this work, we applied this technique to a joint transit–RV modeling analysis using K2 and TESS photometry, published RV measurements, and new RV measurements obtained using the MAROON-X spectrograph (Seifahrt et al. 2018, 2020, 2022). The goal of this study is to constrain better the planetary masses of V1298 Tau’s four transiting planets. In Section 2, we describe the photometric and RV measurements that were taken and included in our analysis. In Sections 3 and 4 we present the methods with which the analysis was carried out and the resulting planetary property constraints (mass, radius, etc.). In Section 5, we discuss the results and their potential implications for theories of planetary formation, evolution, and atmospheric mass loss.

## 2. Observations

### 2.1. Photometry

Multiple transits of V1298 Tau b, c, and d and a single transit of planet e were previously detected during K2 Campaign 4 (David et al. 2019a, 2019b). The data set consists of 3397 data points obtained over a 71 day interval from 2015 February 8 to 2015 April 20 with exposure times of  $\approx 29$  minutes. We include these measurements in our analysis via the EVEREST 2.0 K2 light curve (Luger et al. 2018) that was subsequently cleaned and published by Suárez Mascareño et al. (2021).

Feinstein et al. (2022) reported the detection of the transits of V1298 Tau b, c, d, and e using the publicly available TESS Sectors 43 and 44 data sets (Ricker et al. 2014). The measurements span an  $\approx 50$  day time period from 2021 September 16 to 2021 November 5 with cadences of 20 s and 2 minutes. We used the 2 minutes cadence PDCSAP\_FLUX light curve (Jenkins et al. 2016) available on the MAST archive,<sup>13</sup> which, after removing all data points with NaN values and with quality flags  $\geq 10$ , consists of 31,341 measurements. Each of the four segments were then roughly detrended individually using a linear fit. The light curve was then binned into 10 minute bins yielding a total of 6279 data points. We searched the binned light curve for significant flares by eye and ultimately masked out five points associated with a single flare event occurring at BJD = 2459492.325.

In addition to the K2 and TESS light curves we also used the V-band light curve obtained with the Las Cumbres Observatory (LCOGT) network and published by Suárez Mascareño et al. (2021). The light curves consist of 251 measurements obtained with a cadence of 8 hr from 2019 October 26 to 2020 March

22. The photometric precision is reportedly  $\sim 10$  ppt and is used to provide additional constraints on the stellar activity.

### 2.2. RVs

The RV measurements included in this work were obtained using five instruments. A total of 261 measurements published by Suárez Mascareño et al. (2021) were obtained from 2019 March 1 to 2020 March 29 using HARPS-N (135 measurements with a median uncertainty of  $\bar{\sigma}_{\text{RV}} = 8.9 \text{ m s}^{-1}$ ), CARMENES (33 measurements;  $\bar{\sigma}_{\text{RV}} = 14.8 \text{ m s}^{-1}$ ), SES (57 measurements;  $\bar{\sigma}_{\text{RV}} = 117 \text{ m s}^{-1}$ ), and HERMES (36 measurements;  $\bar{\sigma}_{\text{RV}} = 50.2 \text{ m s}^{-1}$ ; for further details see Suárez Mascareño et al. 2021). We also include 48 new spectroscopic measurements obtained from 2021 August 12 to 2021 November 23 using the MAROON-X spectrograph (Seifahrt et al. 2018, 2020, 2022) installed at the Gemini-North telescope. Two sets of RV measurements were derived from the blue and red arms of the instrument using SERVAL (Zechmeister et al. 2018). The analysis yielded median RV precisions of  $5.9 \text{ m s}^{-1}$  and  $10.3 \text{ m s}^{-1}$  for the blue and red arms, respectively.

## 3. Analysis

A joint modeling analysis of the photometric and RV measurements (described in Section 2) was carried out using tools built into the *exoplanet* Python package (Foreman-Mackey et al. 2021). The adopted two-component models consist of (1) a GP to account for stellar activity and instrumental noise along with (2) models for the planet-induced signatures (transits or stellar reflex RV variations).

### 3.1. Photometric Modeling

The stellar activity and instrumental noise were modeled using a GP implemented with *celerite2* (Foreman-Mackey et al. 2017; Foreman-Mackey 2018). We adopted a kernel consisting of two stochastically driven damped simple harmonic oscillator (SHO) terms centered on the stellar rotation period ( $P_{\text{rot}}$ ) and it is first harmonic. This kernel is characterized by a power spectral density (Equation (20) of Foreman-Mackey et al. 2017) given by

$$S(\omega) = \sqrt{\frac{2}{\pi}} \sum_{n=1}^2 \frac{S_n \omega_n^4}{(\omega^2 - \omega_n^2)^2 + \omega_n^2 \omega^2 / Q^2}, \quad (1)$$

where

$$S_1 = \frac{A^2}{\omega_1 Q}, \quad S_2 = f_{\text{mix}} \frac{A^2}{\omega_2 Q}, \quad \text{and} \quad \omega_n = \frac{2\pi n}{P_{\text{rot}}}. \quad (2)$$

Here,  $\omega_n$  corresponds to the undamped angular frequency of the oscillations;  $S_1$  and  $S_2$  determine the amplitude of the oscillations at  $P_{\text{rot}}$  and it is first harmonic, where the latter is set with respect to the former using the  $f_{\text{mix}}$  parameter. The quality factor  $Q$  describes how quickly the oscillations will die off, where  $0 < Q < 1/2$  leads to overdamped oscillations and a broad power spectral density while  $Q > 1/2$  leads to underdamped oscillations and a sharper power spectral density (see Figure 1 of Foreman-Mackey et al. 2017). Following David et al. (2019b), we force the kernel to be underdamped by reparameterizing  $Q$  as

$$Q = \frac{1}{2} + Q_0 \quad (3)$$

<sup>13</sup> <https://mast.stsci.edu/portal/Mashup/Clients/Mast/Portal.html>

and sampling  $Q_0$  in log space. The diagonal elements of the covariance matrix include contributions from the individual measurement uncertainties ( $\sigma_i$ ) and a jitter term that accounts for additional sources of white noise ( $\sigma_{\text{jit}}^2$ ), which are added in quadrature (i.e.,  $\sqrt{\sigma_i^2 + \sigma_{\text{jit}}^2}$ ).

Unique  $A$ ,  $f_{\text{mix}}$ ,  $P_{\text{rot}}$ ,  $Q_0$ , and  $\sigma_{\text{jit}}$  hyperparameters were assigned to each light curve. We fixed the  $\sigma_{\text{jit}}$  parameter assigned to the K2 photometry to the in-transit white noise level estimated by David et al. (2019b) of 360 ppm. For the TESS photometry, we use a fixed jitter based on a conservative estimate of the in-transit jitter of 850 ppm. This was estimated by first fitting the K2 and TESS light curves individually while including  $\sigma_{\text{jit}}$  as a free parameter. The maximum a posteriori solution yielded  $\sigma_{\text{jit}}^{\text{TESS}}/\sigma_{\text{jit}}^{\text{K2}} \approx 2.36$ , which was then used to estimate the in-transit TESS noise level of  $\sigma_{\text{jit}}^{\text{TESS}} = 850$  ppm. No transits are detectable in the LCOGT photometry due to the lower precision and longer cadence; therefore,  $\sigma_{\text{jit}}^{\text{LCOGT}}$  was set as a free parameter.

The planetary transit component was generated using a `starry` analytic light-curve model (Luger et al. 2019). The model is parameterized by the stellar mass ( $M_*$ ) and radius ( $R_*$ ) along with each planet’s orbital period ( $P$ ), midtransit time ( $T_0$ ), planet–star radii ratio ( $R_p/R_*$ ), impact parameter ( $b$ ), eccentricity ( $e$ ), and argument of periastron ( $\omega$ ). Unique sets of limb-darkening constants ( $u_1$  and  $u_2$ ) are used for the K2 and TESS light curves (sampled using the  $q_1$  and  $q_2$  parameterization recommended by Kipping 2013). For the  $e \geq 0$  model,  $e$  and  $\omega$  are reparameterized by sampling in  $\sqrt{e} \cos \omega$  and  $\sqrt{e} \sin \omega$ , where  $\omega$  corresponds to the host star; we then applied a prior on the eccentricity based on the empirical multiplanet  $e$  distribution published by Van Eylen et al. (2019).

In addition to each light curve’s set of GP hyperparameters, we also include zero-point offset terms ( $\langle f \rangle$ ). TESS has a significantly larger pixel size relative to Kepler ( $\approx 21$  arcsec  $\text{pxl}^{-1}$  compared with  $\approx 4$  arcsec  $\text{pxl}^{-1}$ ), which can potentially introduce contamination from background sources that may alter the transit depths measured between the two instruments. In order to account for this, we initially included a flux-dilution term that scales the planetary component flux associated with the K2 light curve; however, no evidence of dilution was found based on this factor being  $\sim 1$  so the parameter was removed from the subsequent fits.

### 3.2. RV Modeling

Modeling of the five RV data sets was carried out using the same framework that was used for the photometric modeling: the stellar activity and instrumental noise were modeled using GPs in conjunction with models describing the planetary contributions to the stellar RV variations. As noted by previous RV studies of young, active systems, the accuracy with which the stellar activity can be modeled with GPs can be sensitive to the choice of covariance function (e.g., Benatti et al. 2021; Suárez Mascareño et al. 2021). Based on injection–recovery tests that we carried out (see Appendix A.1 in the Appendix), we found that the SHO kernel (Equation (1)) yielded relatively poor accuracy for planets b, d, and e and significantly underestimated the semiamplitudes of planet d’s injected signals. The highest overall accuracy was achieved by adopting the quasi-periodic

kernel (Equation (3.21) of Roberts et al. 2013)

$$k(\tau) = A^2 \exp \left[ -\frac{\sin^2(\pi\tau/P_{\text{rot}})}{2\lambda_p^2} - \frac{\tau^2}{\lambda_e^2} \right], \quad (4)$$

where  $\tau$  is the difference in time between any two data points,  $A$  is the amplitude,  $\lambda_p$  is a dimensionless length scale that specifies the complexity of the periodic variations (lower  $\lambda_p$  implies greater complexity), and  $\lambda_e$  is the exponential decay timescale. Individual measurement uncertainties and jitter terms were included as contributions to the covariance matrix diagonal elements using the same approach used for the photometric GP activity model. Each RV data set was assigned unique  $A$  and  $\sigma_{\text{jit}}$  terms. Two sets of  $P_{\text{rot}}$ ,  $\lambda_p$ , and  $\lambda_e$  terms were used: one set was assigned to the RV measurements published by Suárez Mascareño et al. (2021) and the second set were assigned to the MAROON-X red and blue arm measurements, which were obtained  $\approx 2$  yr after the HARPS and CARMENES measurements.

The stellar reflex RV variations induced by each planet’s Keplerian orbit were modeled using the `RadVel` Python package (Fulton et al. 2018) incorporated into `exoplanet`. The models are parameterized using the systemic or mean center-of-mass velocity ( $\gamma_0$ ), the planet mass  $M_p$  (converted into an RV semiamplitude based on the specified  $M_*$ ,  $P$ , and  $e$ ),  $P$ ,  $T_0$  (converted to the time of periastron),  $e$ , and  $\omega$ .

### 3.3. NUTS HMC Sampling

Posterior distributions for the various model parameters were derived using the Hamiltonian Markov Chain (HMC)-based No-U-Turn Sampler (NUTS) algorithm (Hoffman & Gelman 2014). This was carried out by initializing two chains and adapting the step sizes for a target acceptance rate of 0.95 using 2000 tuning steps (the acceptance rate was increased to 0.97 for the eccentric orbit modeling in order to avoid divergences). After discarding the tuning steps, 10,000 draws were made yielding a total of 20,000 samples combined from the two chains. Convergence was tested using the  $\hat{R}$  statistic (Gelman & Rubin 1992), which was determined to be  $< 1.01$  for all cases presented in this work. Priors adopted for the fitting parameters are listed in Table 1.

### 3.4. Four-planet Model

Multiple transits of V1298 Tau b, c, and d have been detected in both the K2 and TESS light curves (David et al. 2019b; Feinstein et al. 2022); the transit of planet e, on the other hand, was only detected once in each of these data sets. Suárez Mascareño et al. (2021) report the detection of an RV signal having a period of  $40.2 \pm 1.0$  days and a semiamplitude of  $62_{-16}^{+15}$   $\text{m s}^{-1}$ , which they attribute to planet e. While the 40.2 days period is consistent with the detected K2 transit of planet e, it is inconsistent with the new period lower limit placed by the TESS transit. Feinstein et al. (2022) note that the possible orbital periods for e have a lower bound of  $P_e > 42.7$  days, which corresponds to the time between the observed TESS transit and the last TESS measurement. Therefore, assuming circular Keplerian orbits (i.e., ignoring any transit timing variations (TTVs)) and considering only the timing of the observed transits, there are a total of 55 discrete solutions for planet e’s period given by

$$P_e \approx \Delta T_e / n_e \quad \text{for } n_e = 1, \dots, 55, \quad (5)$$

**Table 1**  
Planetary, Stellar, and Additional Model Parameters Derived Using the  $n_e = 51$  Solution ( $P_e \approx 46.8$  days)

| Parameter                                       | c                                 | d                              | b  | e                            |                              |                        |
|---|-----------------------------------|--------------------------------|--|------------------------------|------------------------------|------------------------|
| $T_0 - 2454833$                                 | 2231.2822(22)                     | 2239.3943(17)                  | 2234.0481(12)                                  | 2263.6222(27)                |                              |                        |
| $P$ [days]                                      | 8.248720(24)                      | 12.402140(17)                  | 24.140410(22)                                  | 46.768131(76)                |                              |                        |
| $b$   | <0.36                             | <0.35                          | $0.451^{+0.033}_{-0.030}$                      | $0.595^{+0.025}_{-0.024}$    |                              |                        |
| $a/R_*$   | $13.32^{+0.20}_{-0.24}$           | $17.48^{+0.26}_{-0.32}$        | $27.25^{+0.40}_{-0.49}$                        | $42.35^{+0.62}_{-0.77}$      |                              |                        |
| $R_p/R_*$                                       | $0.0354 \pm 0.0013$               | $0.0429^{+0.0016}_{-0.0017}$   | $0.0673 \pm 0.0017$                            | $0.0643 \pm 0.0029$          |                              |                        |
| $K$ [ $\text{m s}^{-1}$ ]                       | $5.7 \pm 2.6$                     | <9.0                           | <32  | $34 \pm 13$                  |                              |                        |
| $M_p/M_* \times 10^4$                           | $0.52^{+0.24}_{-0.23}$            | <0.94                          | <4.1   | $5.5 \pm 2.1$                |                              |                        |
| $i$ [deg]                                       | >88.39                            | >88.80                         | $89.052^{+0.072}_{-0.087}$                     | $89.195^{+0.040}_{-0.044}$   |                              |                        |
| $a$ [au]  | $0.0839 \pm 0.0014$               | $0.1101^{+0.0018}_{-0.0019}$   | $0.1716^{+0.0028}_{-0.0029}$                   | $0.2667^{+0.0043}_{-0.0045}$ |                              |                        |
| $T_{14}$ [hr]                                   | $4.826^{+0.080}_{-0.087}$         | $5.596^{+0.063}_{-0.081}$      | $6.547^{+0.070}_{-0.068}$                      | $7.45^{+0.12}_{-0.11}$       |                              |                        |
| $T_{\text{eq}}$ [K]                             | $979 \pm 21$                      | $855 \pm 19$                   | $685 \pm 15$                                   | $549 \pm 12$                 |                              |                        |
| $R_p$ [ $R_{\text{Jup}}$ ]                      | $0.467 \pm 0.021$                 | $0.566^{+0.027}_{-0.026}$      | $0.888^{+0.033}_{-0.031}$                      | $0.848^{+0.046}_{-0.044}$    |                              |                        |
| $R_p$ [ $R_{\oplus}$ ]                          | $5.24^{+0.24}_{-0.23}$            | $6.34 \pm 0.30$                | $9.95^{+0.37}_{-0.35}$                         | $9.50^{+0.51}_{-0.49}$       |                              |                        |
| $M_p$ [ $M_{\text{Jup}}$ ]                      | $0.062^{+0.029}_{-0.028}$         | <0.114                         | <0.50  | $0.66 \pm 0.26$              |                              |                        |
| $M_p$ [ $M_{\oplus}$ ]                          | $19.8^{+9.3}_{-8.9}$              | <36                            | <159   | $210 \pm 82$                 |                              |                        |
| $\rho_p$ [ $\text{g cm}^{-3}$ ]                 | $0.76^{+0.38}_{-0.35}$            | <0.81                          | <0.90  | $1.33^{+0.59}_{-0.53}$       |                              |                        |
| Parameter                                       |                                   |                                |  |                              |                              |                        |
| $M_*$ [ $M_{\odot}$ ]                           | $1.157^{+0.057}_{-0.058}$         |                                |  |                              |                              |                        |
| $R_*$ [ $R_{\odot}$ ]                           | $1.355^{+0.032}_{-0.030}$         |                                |  |                              |                              |                        |
| $T_{\text{eff}}$ [K]                            | $5050 \pm 100$                    |                                |  |                              |                              |                        |
| Parameter                                       |                                   |                                |  |                              |                              |                        |
|   | K2                                | TESS                           | LCOGT  |                              |                              |                        |
| $u_1$   | $0.40 \pm 0.18$                   | $0.46^{+0.23}_{-0.26}$         |  |                              |                              |                        |
| $u_2$   | <0.60                             | $0.29^{+0.24}_{-0.27}$         |  |                              |                              |                        |
| $\langle f \rangle$ [ppt]                       | $0.02 \pm 0.31$                   | $0.12 \pm 0.61$                | $1.48 \pm 0.54$                                |                              |                              |                        |
| $\ln P_{\text{tot}}$ [days]                     | $1.0541 \pm 0.0082$               | $1.058^{+0.027}_{-0.031}$      | $1.0682 \pm 0.0012$                            |                              |                              |                        |
| $\ln A$ [ppt]                                   | $-2.44^{+0.40}_{-0.31}$           | $-3.85 \pm 0.34$               | $0.19^{+0.94}_{-0.75}$                         |                              |                              |                        |
| $\ln f_{\text{mix}}$                            | $0.50^{+0.67}_{-0.53}$            | $0.61^{+0.48}_{-0.47}$         | $-2.95^{+0.79}_{-0.91}$                        |                              |                              |                        |
| $\ln Q_0$                                       | $3.05^{+0.80}_{-0.52}$            | $0.59^{+0.30}_{-0.27}$         | $6.25^{+0.97}_{-0.82}$                         |                              |                              |                        |
| $\ln \sigma_{\text{jit}}$ [ppt]                 |                                   |                                | $1.92^{+0.08}_{-0.11}$                         |                              |                              |                        |
| Parameter                                       |                                   |                                |  |                              |                              |                        |
|   | HARPS-N                           | CARMENES                       | STELLA   | HERMES                       | MX (blue)                    | MX (red)               |
| $\gamma_0$                                      | $-2.1^{+9.9}_{-10.0}$             | $-0.8^{+9.7}_{-9.8}$           | $-1 \pm 10$                                    | $-0.6^{+9.9}_{-9.8}$         | $-0.6^{+9.8}_{-9.9}$         | $-1.1^{+9.8}_{-9.5}$   |
| $\ln A_1$ [ $\text{m s}^{-1}$ ]                 | $5.41^{+0.11}_{-0.10}$            | $5.43^{+0.15}_{-0.16}$         | $5.63 \pm 0.16$                                | $5.95^{+0.19}_{-0.18}$       | $5.31^{+0.23}_{-0.22}$       | $4.72^{+0.18}_{-0.16}$ |
| $\ln P_{\text{tot}}$ [days]                     | $1.0636^{+0.0014}_{-0.0015}$      |                                |  |                              | $1.0728^{+0.0079}_{-0.0076}$ |                        |
| $\ln \lambda_e$                                 | $3.17^{+0.09}_{-0.10}$            |                                |  |                              | $1.94^{+0.17}_{-0.13}$       |                        |
| $\ln \lambda_p$                                 | $-1.171^{+0.082}_{-0.079}$        |                                |  |                              | $-1.34^{+0.24}_{-0.29}$      |                        |
| $\ln \sigma_{\text{jit}}$ [ $\text{m s}^{-1}$ ] | $2.79^{+0.16}_{-0.18}$            | $1.4^{+1.7}_{-2.4}$            | $2.1^{+1.3}_{-2.0}$                            | $3.8^{+0.5}_{-1.7}$          | $1.7^{+1.1}_{-2.7}$          | $1.7^{+1.0}_{-2.6}$    |
| Parameter                                       |                                   |                                |  |                              |                              |                        |
|   | Prior                             | Parameter                      | Prior  | Parameter                    | Prior                        |                        |
| $\ln T_0/d$                                     | $\mathcal{N}(\ln T_0, 0.01)^a$    | $R_*/R_{\odot}$                | $\mathcal{N}(1.278, 0.07)^b$                   | $\ln A$                      | $\mathcal{U}[-10, 10]$       |                        |
| $\ln P/d$                                       | $\mathcal{N}(\ln P, 0.01)^a$      | $q_1^c$                        | $\mathcal{U}[0, 1]$                            | $\ln f_{\text{mix}}$         | $\mathcal{U}[-5, 5]$         |                        |
| $b$   | $\mathcal{U}[0, 1 + R_p/R_*]$     | $q_2^c$                        | $\mathcal{U}[0, 1]$                            | $\ln Q_0$                    | $\mathcal{N}(1, 10)$         |                        |
| $\ln R_p/R_*$                                   | $\mathcal{N}(\ln R_p/R_*, 0.1)^a$ | $\langle f \rangle/\text{ppt}$ | $\mathcal{N}(0, 10)$                           | $\gamma_0/[\text{m s}^{-1}]$ | $\mathcal{N}(0, 10)$         |                        |
| $\ln M_p/M_{\oplus}$                            | $\mathcal{U}[0, 7.37]$            | $\ln \sigma_{\text{jit}}$      | $\mathcal{N}(\ln \langle \sigma_i \rangle, 3)$ | $\ln \lambda_e$              | $\mathcal{U}[0, 10]$         |                        |
| $M_*/M_{\odot}$                                 | $\mathcal{N}(1.17, 0.06)^b$       | $\ln P_{\text{tot}}/d$         | $\mathcal{U}[1.0, 1.1]$                        | $\ln \lambda_p$              | $\mathcal{U}[-5, 1]$         |                        |

**Notes.** The adopted values correspond to the median, the errors are  $1\sigma$  (taken to be the 15.9 and 84.1 percentiles), and the upper/lower limits correspond to  $2\sigma$  (2.3 and 97.7 percentiles). The equilibrium temperatures ( $T_{\text{eq}}$ ) are calculated assuming zero albedo. Note that the mass constraints derived for planet d are likely underestimated by 10%–15% based on the injection–recovery tests presented in Appendix A.1 of the Appendix. The values presented in parentheses correspond to the uncertainty in the last digit.

<sup>a</sup> TTV analysis where  $(T_{0,b}, P_b) = (2234.048, 24.140)$ ,  $(T_{0,c}, P_c) = (2231.280, 8.249)$ ,  $(T_{0,d}, P_d) = (2239.396, 12.402)$ , and  $(T_{0,e}, P_e) = (2263.620, 43.367)$ .

<sup>b</sup> Suárez Mascareño et al. (2021).

<sup>c</sup> Parameterization of  $u_1$  and  $u_2$  from Kipping (2013).

<sup>d</sup> David et al. (2019a).

where  $\Delta T_e$  is defined as the difference between the TESS and K2 transit times ( $\text{BJD}_e^{\text{TESS}} - \text{BJD}_e^{\text{K2}} \approx 6.5$  yr) and  $n_e = 55$  corresponds to the shortest period that remains  $>42.7$  days.

We derived solutions for all of the  $P_e$  values defined by Equation (5) using all of the available RV and photometric data sets. This was done by adopting narrow priors centered on each  $P_e$  value being considered.<sup>14</sup> For expediency, we initially assumed circular orbits, which we note causes planet e’s impact parameter ( $b_e$ ) to increase with decreasing  $n_e$  such that  $b_e$  approaches 1 for  $n_e \lesssim 20$  ( $P_e \gtrsim 119$  days).

### 3.5. Transit Times

Individual transit times associated with each of the K2 and TESS transits identified by David et al. (2019b) and Feinstein et al. (2022), respectively, were derived using the general framework described above. The two data sets were modeled simultaneously (without the inclusion of the RVs or the LCOGT light curve) using the `TTVOrbit` class of the `exoplanet` package, which introduces an additional free parameter for each transit event that specifies its time of occurrence. We adopted normal prior distributions for each transit time with mean values calculated using the published K2 ephemerides (David et al. 2019b) and TESS ephemerides (Feinstein et al. 2022) and with a standard deviation of 0.05 days; we tested whether the derived posteriors are sensitive to the adopted prior width by increasing this width by a factor of 10, which did not have a noticeable impact. For planet e, transit indices were specified in the `TTVOrbit` class assuming  $n_e = 51$  ( $P_e \approx 44$  days in Equation (5)), which corresponds to the most probable  $n_e$  derived later in the analysis (Section 4.2 below). The transit times were initially estimated assuming  $n_e = 54$ , which yielded similar results.

## 4. Results

### 4.1. Transit Times

In Table 2, we list the transit times and observed-minus-calculated ( $O - C$ ) values determined from the derived posterior distributions. Reported values correspond to each distribution’s median value and the uncertainties correspond to 15.9 and 84.1 percentiles. Average uncertainties in the transit times for planets b, c, d, and e range from  $\approx 0.003$  to 0.012 days;  $O - C$  uncertainties of planets b, c, and d are approximately 3, 16, and 8 minutes, respectively.

In Figure 1, we show the  $O - C$  values associated with the derived transit times for planets b, c, and d. Some of the transit times and their estimated uncertainties are impacted by biases that can be attributed to instances of coincident transit events (e.g., planet c’s fifth transit and d’s third transit in the K2 data) or partial event coverage (e.g., planet b’s third transit). In total, nine of the 31 transit times derived from the K2 and TESS photometry may be affected by such biases (two for planet b, four for planet c, and three for planet d). No clear evidence of TTVs is obtained from our analysis (regardless of whether or not the potentially biased transit times are considered), which is consistent with the findings of David et al. (2019b) and Feinstein et al. (2022). As a result, the joint transit–RV modeling analysis presented below, which was conducted

<sup>14</sup> The impact of the chosen narrow priors in both  $P$  and  $T_0$  (see Table 1) was tested by increasing the width of these priors by a factor of 10; the derived posteriors were not found to be noticeably impacted.

**Table 2**  
Transit Times ( $\text{BJD}_{\text{TT}}$ ) and  $O - C$  Times Derived from the K2 and TESS Light Curves

| Planet                       | $\text{BJD}_{\text{TT}}$<br>– 2454833        | $O - C$<br>(minutes) |
|------------------------------|--|----------------------|
| b                            | $2234.0483^{+0.0016}_{-0.0019}$              | $0.7^{+2.5}_{-2.6}$  |
|                              | $2258.1897^{+0.0025}_{-0.0022}$              | $2.4^{+3.0}_{-2.8}$  |
|                              | <sup>a</sup> $2282.3265^{+0.0029}_{-0.0034}$ | $-3.1^{+3.2}_{-3.6}$ |
|                              | <sup>a</sup> $4648.0893^{+0.0028}_{-0.0029}$ | $0.2 \pm 2.7$        |
|                              | $4672.2295 \pm 0.0025$                       | $-0.1 \pm 2.7$       |
| c                            | $2231.2786^{+0.0067}_{-0.0077}$              | $-4^{+10}_{-11}$     |
|                              | <sup>a</sup> $2239.5287^{+0.0064}_{-0.0052}$ | $-2^{+10}_{-9}$      |
|                              | $2247.7775^{+0.0086}_{-0.0066}$              | $-1^{+12}_{-9}$      |
|                              | $2256.0339^{+0.0070}_{-0.0066}$              | $9^{+10}_{-9}$       |
|                              | <sup>a</sup> $2264.2536^{+0.0056}_{-0.0086}$ | $-33^{+7}_{-10}$     |
|                              | $2272.5285^{+0.0070}_{-0.0074}$              | $5 \pm 10$           |
|                              | $2280.794^{+0.011}_{-9}$                     | $31^{+13}_{-9}$      |
|                              | <sup>a</sup> $2289.0184^{+0.0049}_{-0.0053}$ | $-5.8^{+6.5}_{-6.8}$ |
|                              | $2297.2700^{+0.0057}_{-0.0068}$              | $-1.9^{+8.0}_{-8.9}$ |
|                              | <sup>a</sup> $4648.1627^{+0.0067}_{-0.0084}$ | $7^{+14}_{-16}$      |
|                              | $4656.399^{+0.031}_{-0.013}$                 | $-6^{+34}_{-22}$     |
|                              | $4664.652^{+0.023}_{-0.014}$                 | $-2^{+28}_{-21}$     |
|                              | $4672.897^{+0.010}_{-0.011}$                 | $-11^{+16}_{-20}$    |
| $4681.156^{+0.028}_{-0.025}$ | $6^{+34}_{-31}$                              |                      |
| $4689.398^{+0.016}_{-0.010}$ | $-3^{+21}_{-17}$                             |                      |
| d                            | <sup>a</sup> $2239.3925^{+0.0034}_{-0.0036}$ | $-6.3^{+5.0}_{-5.2}$ |
|                              | $2251.7922^{+0.0034}_{-0.0042}$              | $-9.9^{+5.0}_{-5.7}$ |
|                              | <sup>a</sup> $2264.2002^{+0.0087}_{-0.0058}$ | $-1^{+10}_{-7}$      |
|                              | $2276.5974^{+0.0045}_{-0.0042}$              | $-8.1^{+5.9}_{-5.7}$ |
|                              | <sup>a</sup> $2289.0224^{+0.0032}_{-0.0034}$ | $24.6^{+4.8}_{-5.0}$ |
|                              | $4645.4104^{+0.0030}_{-0.0067}$              | $2.5^{+6.8}_{-8.3}$  |
|                              | $4657.8161^{+0.0066}_{-0.0044}$              | $8.6^{+7.9}_{-6.1}$  |
|                              | $4670.2136^{+0.0055}_{-0.0045}$              | $1.6^{+7.1}_{-6.3}$  |
| e                            | $2263.6224^{+0.0028}_{-0.0027}$              | 0                    |
|                              | $4648.7969 \pm 0.0029$                       | 0                    |

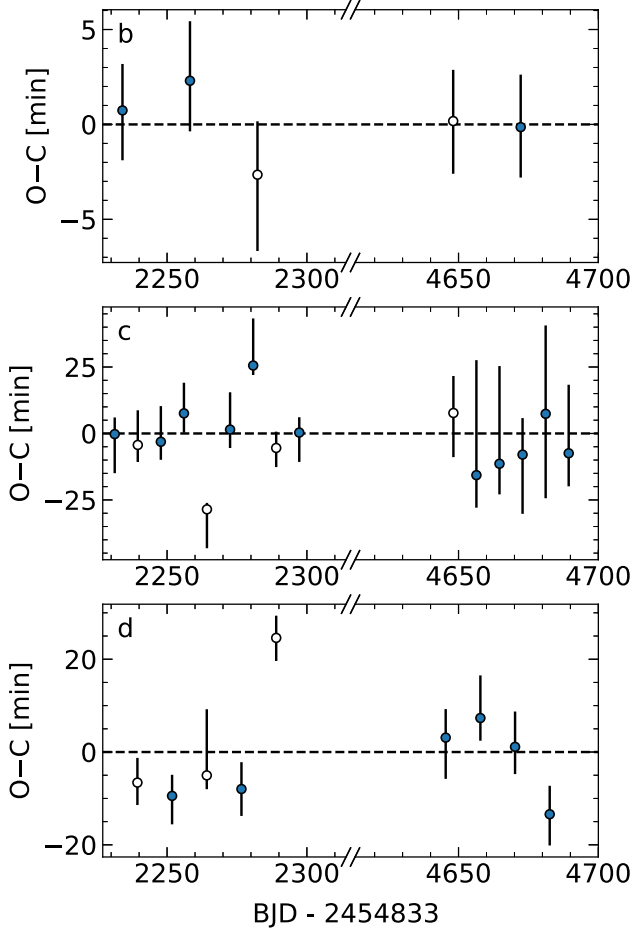
**Notes.** Gaussian priors on  $\text{BJD}_{\text{TT}}$ —centered on the transit times associated with the ephemerides published by David et al. (2019a) and Feinstein et al. (2022)—with standard deviations of 0.05 days were adopted.

<sup>a</sup> Overlapping transits or partial event coverage.

using all of the publicly available data sets and the new MAROON-X data, assumed Keplerian orbits and used Gaussian priors for the orbital periods centered on the mean periods derived from this transit timing analysis. We note, however, that additional transit observations do exhibit significant TTVs (J. Livingston et al. 2023, in preparation); the fact that we do not find evidence of TTVs in the K2 or TESS light curves can be attributed to the  $\approx 4.5$  yr superperiod describing the TTVs for planets c and d as predicted by David et al. (2019b) and the fact that the two data sets were likely obtained during low TTV amplitude phases of this superperiod. The ephemerides reported in this work should therefore be used with caution in regards to future transit timing predictions.

### 4.2. Orbital Period of Planet e

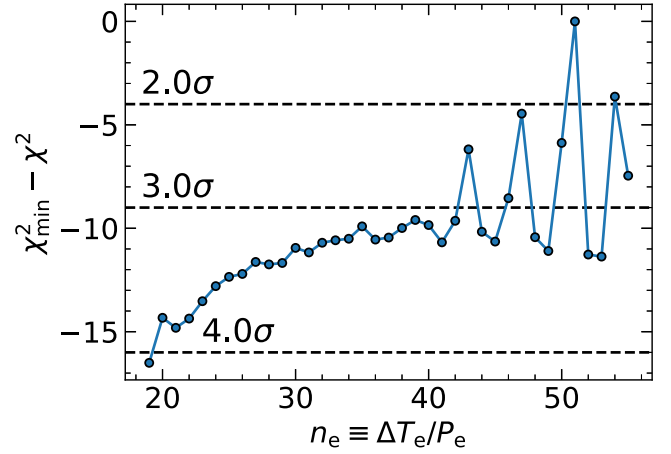
The constraints on  $P_e$  given by Equation (5) are based only on the timing of the two observed transits within the K2 and TESS light curves. In order to determine whether the joint light



**Figure 1.**  $O - C$  values for the derived transit times measured with respect to each planet’s  $\langle P \rangle$ ; the break in the x-axis separates the K2 measurements (BJD – 2454833 < 2300) from the TESS measurements (BJD – 2454833 > 4640). The white points are those measurements that may be biased due to overlapping transits or partial event coverage.

curve and RV analysis provides additional constraints on  $P_e$  (i.e., on  $n_e \equiv \Delta T_e / P_e$ ), we compared the  $\chi^2$  values associated with each of the 36  $P_e$  solutions that we considered. Each  $\chi^2$  value was calculated using the median of the log-likelihood distributions obtained from the sampling analysis. We found that the solution that yielded the lowest  $\chi^2$  is defined by  $n_e = 51$  ( $P_e = 46.768131 \pm 0.000076$  days), which we adopt as the most probable value. In Figure 2, we show the  $\Delta\chi^2 \equiv \chi_{\min}^2 - \chi^2$  values for the tested  $n_e$  solutions calculated with respect to the most probable solution. The seven solutions yielding the lowest  $\chi^2$  values are defined by  $n_e = 43, 46, 47, 50, 51, 54,$  and  $55$  and are consistent within  $3\sigma$ . For longer periods ( $P_e > 55.4$  days),  $\Delta\chi^2$  decreases approximately monotonically with decreasing  $n_e$  (increasing  $P_e$ ) toward  $\Delta\chi^2 < -90$  at  $n_e = 1$ . Below we report the results of the adopted  $n_e = 51$  solution and how the associated mass constraints compare with those of the other six  $P_e$  solutions that cannot be ruled out from the analysis presented in this work at the  $3\sigma$  level.

All of the derived parameters for the  $n_e = 51$  solution are listed in Table 1. In Figures 3–6, we show the median solution fits (i.e., the solution calculated using the median value of each posterior that is listed in Table 1) to the K2 and TESS light curves obtained for the adopted  $n_e = 51$  solution. The associated fits to the RV measurements are shown in



**Figure 2.**  $\Delta\chi^2 \equiv \chi_{\min}^2 - \chi^2$  values associated with each of the  $n_e$  solutions (Equation (5)) found to be consistent with the most probable solution ( $n_e = 51$ ,  $P_e \approx 46.8$  days) at the  $\approx 4\sigma$  level; lower  $n_e$  values, which decrease monotonically toward  $\chi_{\min}^2 - \chi^2 < -90$  at  $n_e = 1$ , are not shown for visual clarity. The  $2\sigma$ ,  $3\sigma$ , and  $4\sigma$  confidence intervals are indicated by the horizontal dashed lines. Under the assumption of circular orbits, all longer periods with  $P_e > 55.4$  days are rejected at the  $3\sigma$  level in favor of the  $n_e = 51$  solution, while seven shorter period solutions with  $43.3 < P_e/d < 55.4$  ( $n_e = 43, 46, 47, 50, 51, 54,$  and  $55$ ) are consistent within  $3\sigma$ .

Figure 7 and the phased RVs showing individual planetary contributions to the measurements are shown in Figure 8.

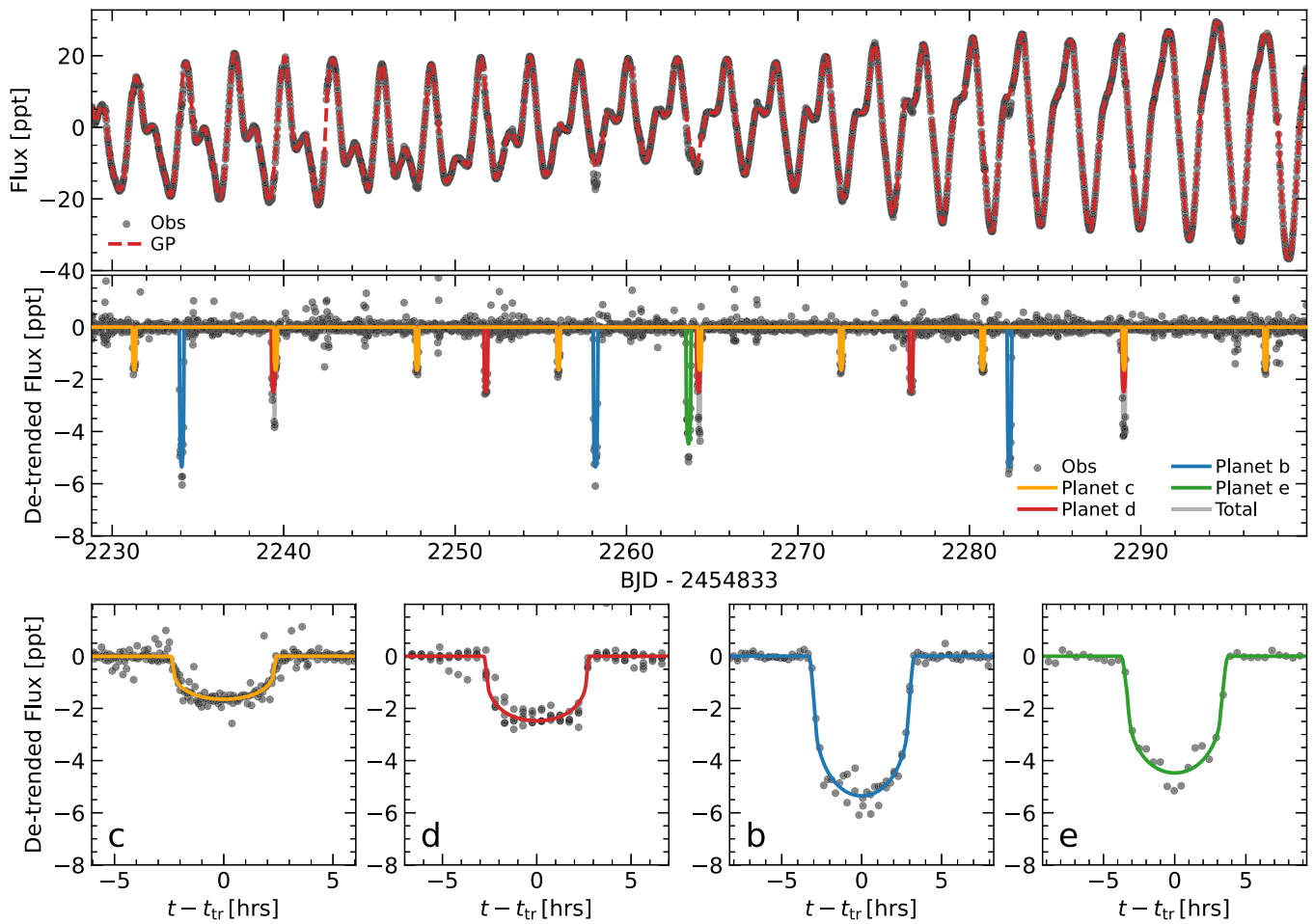
### 4.3. Planetary Masses

In Figure 9 we show the marginalized RV semiamplitude posterior distributions of the four planets derived for all of the seven most probable  $n_e$  solutions (i.e., those within the  $3\sigma$  confidence interval of the  $n_e = 51$  solution) assuming circular orbits. The posteriors of planet e depend strongly on the adopted  $n_e$  value while those of planets b and c are moderately impacted. No clear detections of RV signatures associated with planets b and d are obtained. Weakly significant detections are obtained for planets c and e: planet c is detected with a significance of  $\approx 2\sigma$  (for all  $n_e$  values) and planet e has a maximum detection significance of  $2.6\sigma$ , which is associated with the most probable  $n_e = 51$  solution. A comparable detection significance for planet e (i.e.,  $> 2\sigma$ ) is also obtained for the  $n_e = 43, 47, 50,$  and  $54$  solutions, which, including the  $n_e = 51$  solution, correspond to the five most probable solutions shown in Figure 2.

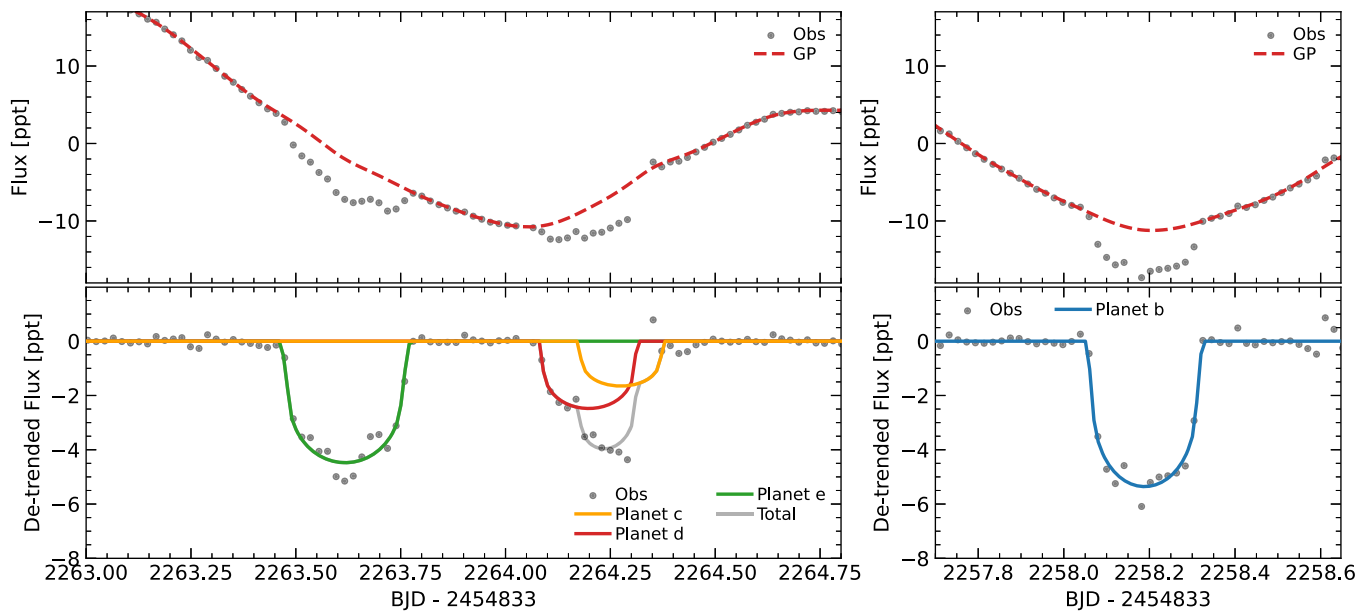
Considering the  $n_e = 51$  solution, we derive  $2\sigma$  upper limits on the semiamplitudes of planets b and d of  $K_b < 32 \text{ m s}^{-1}$  and  $K_d < 9.0 \text{ m s}^{-1}$ , which correspond to upper mass limits of  $M_b < 159 M_{\oplus}$  and  $M_d < 36 M_{\oplus}$ . While the injection–recovery tests that we performed (Appendix A.1 of the Appendix) imply that our model can accurately constrain  $K_b$ ,  $K_c$ , and  $K_e$ , they reveal a systematic bias in which  $K_d$  is underestimated by  $\approx 10\%–15\%$ . Taking this bias into account implies a slightly higher upper limit on planet d’s mass of  $M_d < 41.4 M_{\oplus}$ . For planets c and e, we obtain  $K_c = 5.7 \pm 2.6 \text{ m s}^{-1}$  ( $M_c = 19.8_{-8.9}^{+9.3} M_{\oplus}$ ) and  $K_e = 34 \pm 13 \text{ m s}^{-1}$  ( $M_e = 0.66 \pm 0.26 M_{\text{Jup}}$ ). Considering the seven most probable solutions shown in Figure 9, the  $n_e$  yields the highest upper limits on the masses of planets c and e of  $M_c < 39 M_{\oplus}$  and  $M_e < 1.34 M_{\text{Jup}}$ .

#### 4.3.1. Constraints from Dynamical Stability

The dynamical stability of the adopted solution was evaluated using the Stability of Planetary Orbital Configurations Klassifier



**Figure 3.** Best fit to the K2 light curve using the  $n_e = 51$  ( $P_e \approx 46.8$  days) solution. The top panel shows the observed flux measurements compared with the GP model. The middle panel shows the transit models compared with the detrended measurements (i.e., with the GP model removed). The bottom four panels show the phased transits for planets b, c, d, and e; individual transits are shown in Figure 4.



**Figure 4.** Selected individual transits observed in the K2 light curve.

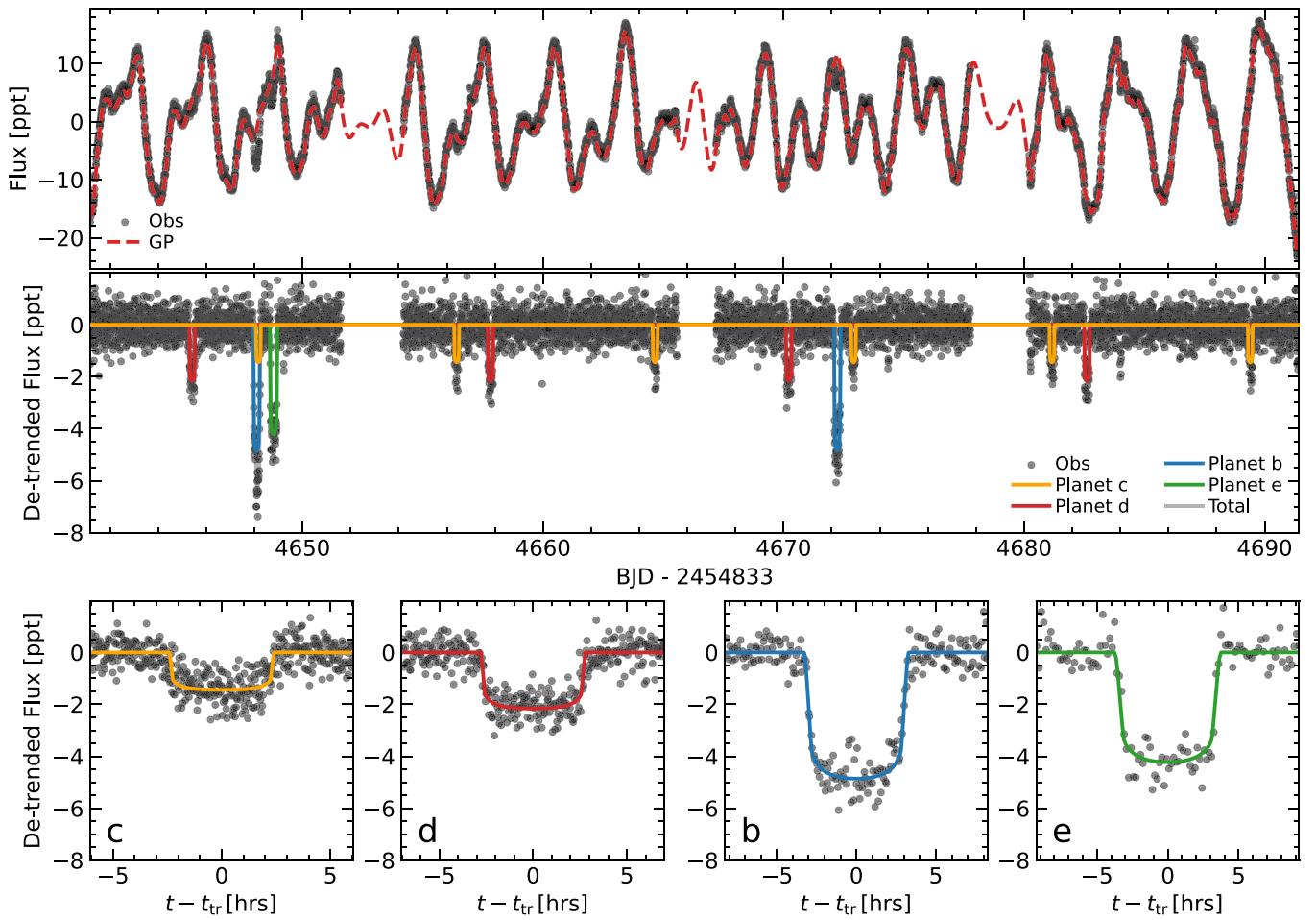


Figure 5. Same as Figure 3 but for the TESS light curve. Individual transits are shown in Figure 6.

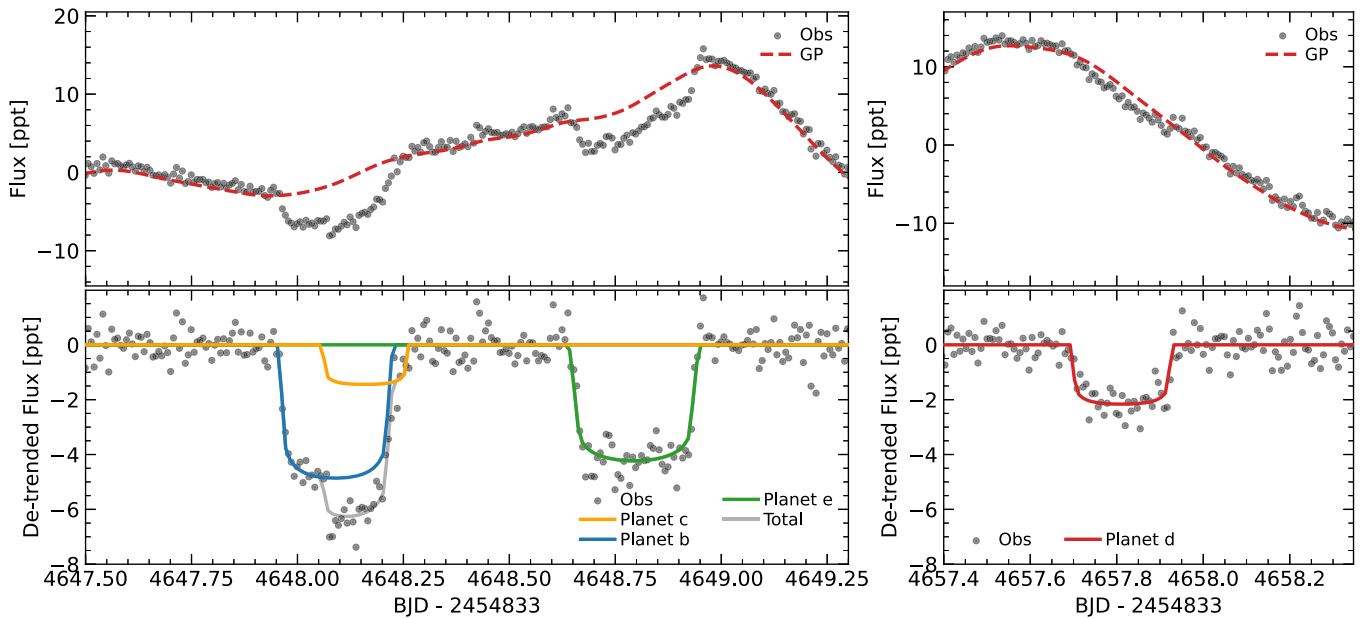
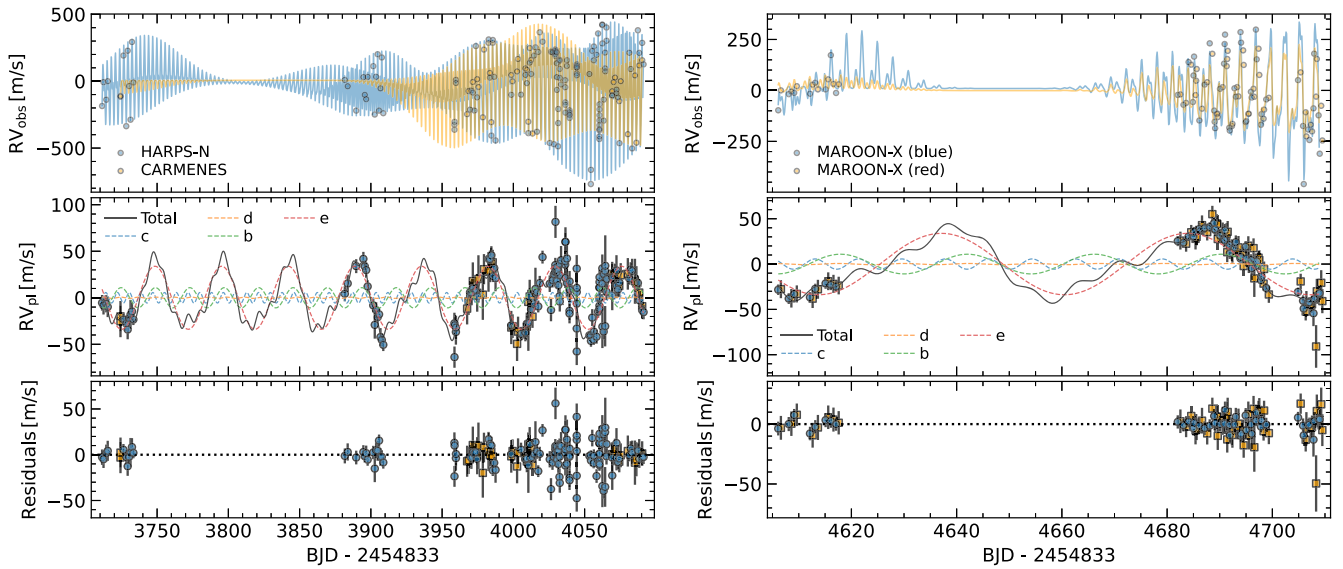


Figure 6. Selected individual transits observed in the TESS light curve.

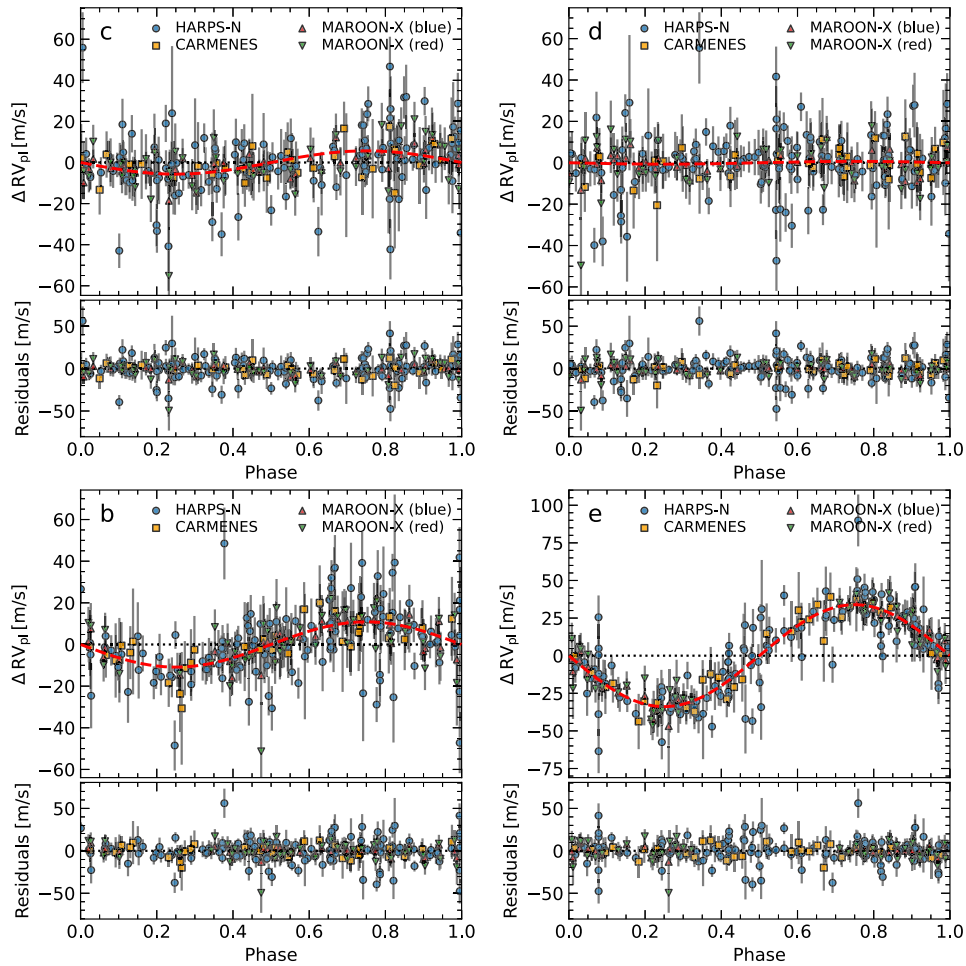
(SPOCK; Tamayo et al. 2020, 2021) Python package. SPOCK is able to estimate quickly the probability that a multiplanet system with a given set of initial conditions will maintain stability over  $10^9$  orbits (i.e.,  $\sim 20$  Myr for V1298 Tau). We calculated this stability probability for each of the posterior samples (i.e., using

$M_*$  along with each planet's  $T_0$ ,  $P$ , inclination angle, mass,  $e$ , and  $\omega$  in the case of noncircular orbits) obtained from the NUTS sampling analysis. In Figure 12 of the Appendix, we show the derived  $M_p$  posteriors along with the stability probabilities calculated with SPOCK (black contours). The stability probability

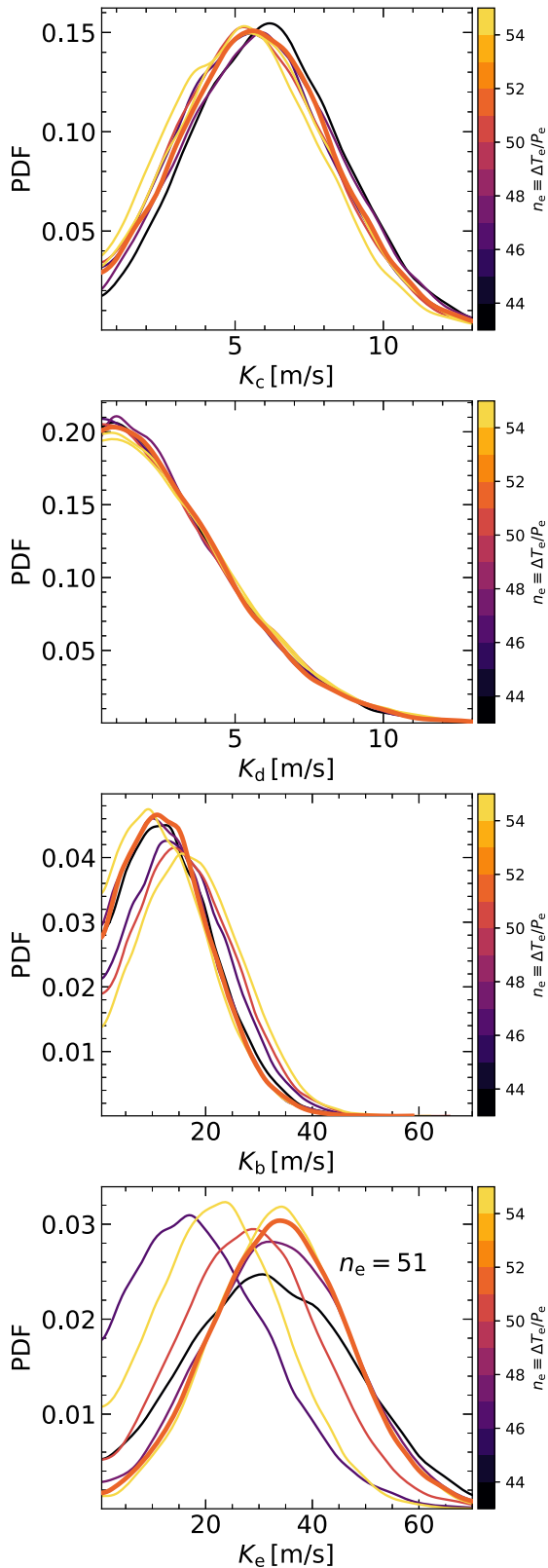




**Figure 7.** Best fit to the HARPS and CARMENES RV measurements (left panels) and the MAROON-X red and blue measurements (right panels) using the  $n_c = 51$  ( $P_c \approx 46.8$  days) solution (n.b., the MAROON-X measurements are plotted with a time offset for better visibility). The top panels show the GP fit to the observed RVs with the planetary component removed, the middle panels show the total planetary component with the GP fit removed, and the bottom panels show the residuals. The STELLA and HERMES measurements, which are included in our analysis, are not shown due to their comparatively large uncertainties.



**Figure 8.** Individual planetary contributions to the stellar reflex RV phased by orbital period for the median solution fit (Table 1) assuming  $P_c \approx 46.8$  days. Filled circles correspond to the detrended observed RVs and the red dashed lines indicate the model fits. For visual clarity, the STELLA and HERMES measurements are not plotted.



**Figure 9.** Marginalized posterior distributions derived for the RV semiamplitudes of planets c, d, b, and e for the seven most probable  $n_c$  solutions—those that are consistent with the most probable  $n_c = 51$  solution ( $P_e \approx 46.8$  days) within the  $3\sigma$  confidence interval. The thicker line indicates the  $n_c = 51$  solution.

distribution is bimodal with peaks occurring at  $\approx 0.33$  and  $\approx 0.65$ . The stability probabilities are most clearly anticorrelated with  $M_b$  with lower mass solutions being more stable. The blue contours

show the distributions after applying rejection sampling to the stability probability distribution, which predominantly removes samples with low stability. This shifts planet b’s  $2\sigma$  upper mass limit down slightly to  $M_b < 141 M_\oplus$  while smaller shifts occur for the other three planets.

#### 4.3.2. Noncircular Orbits

We carried out the same sampling analysis for the  $n_c = 51$  solution presented above but allowing for noncircular orbits. In this case, we derive low eccentricities for planets b, d, and e of  $e_b < 0.13$ ,  $e_d < 0.14$ , and  $e_e < 0.32$ , respectively. The derived masses for these planets are found to be comparable to the circular orbits case:  $M_b < 149 M_\oplus$ ,  $M_d < 39 M_\oplus$ , and  $M_e = 0.70 \pm 0.27 M_{\text{Jup}}$ . Planet c, on the other hand, is found to have a large eccentricity of  $e_c = 0.44^{+0.10}_{-0.12}$  and a notably larger mass of  $39 \pm 11 M_\oplus$ —nearly twice that of the mass derived assuming  $e = 0$ . We calculated the stability probabilities for the posterior samples using SPOCK and find that they have similar distributions to those of the circular orbits case albeit with a small shift in the stability probability of  $\lesssim 0.05$  toward lower probabilities.

The mass and eccentricity posterior distributions along with the calculated distribution of the stability probabilities are shown in Figure 13 of the Appendix. Both planets c and e have bimodal eccentricity posteriors: aside from the most probable eccentricities noted above, the posteriors have peaks with lower relative probabilities at  $e_c \approx 0$  and  $e_e \approx 0.3$ , respectively. When including only the K2 and TESS data sets in the sampling analysis and allowing for noncircular orbits, we obtain low eccentricities for all four planets characterized by  $2\sigma$  upper limits of  $e_b < 0.17$ ,  $e_c < 0.30$ ,  $e_d < 0.12$ , and  $e_e < 0.25$ ; therefore, the high value of  $e_c$  is primarily driven by the RVs. Shen & Turner (2008) show that small, low signal-to-noise ratio RV data sets may be significantly biased toward high eccentricities and high masses. Considering the semiamplitude of planet c’s RV signal ( $K_c = 5.7 \pm 2.6 \text{ m s}^{-1}$ ) and the typical measurement uncertainty of  $\approx 10 \text{ m s}^{-1}$ , we conclude that the lower  $e_c$  and lower  $M_c$  solution is most reliable.

## 5. Discussion and Summary

In this study, we carried out a joint transit and RV modeling analysis of the young V1298 Tau system, which contains four transiting short-period planets with  $4.9\text{--}9.6 R_\oplus$  radii. We include the constraints imposed on planet e’s orbital period by the transit observed with K2, the transit observed with TESS, and the RVs and ultimately obtain at least seven plausible solutions. These solutions have  $43.3 \text{ days} < P_e < 55.4 \text{ days}$  while longer-period solutions ( $43.3 \text{ days} < P_e < 6.54 \text{ yr}$ ) can be ruled out a  $3\sigma$  limit. The most probable solution corresponds to  $P_e = 46.768131 \pm 0.000076$  days and, assuming circular orbits, yields a relatively low-significance  $2.6\sigma$  RV detection of planet e with a mass of  $M_e = 0.66 \pm 0.26 M_{\text{Jup}}$ . In the absence of additional constraints on planet e’s orbital period (i.e., considering the posteriors derived for the seven most probable  $P_e$  values), we obtain a  $2\sigma$  upper limit of  $M_e < 1.34 M_{\text{Jup}}$ .

The mass posteriors derived for planets b, c, and d are approximately independent of the assumed  $P_e$  (small correlations are apparent; see Figure 9). We obtain an  $\approx 2\sigma$  detection of planet c with a mass of  $M_c = 19.8^{+9.3}_{-8.9} M_\oplus$ . For planets b and d, we obtain  $2\sigma$  upper mass limits of  $M_b < 159 M_\oplus$  and  $M_d < 36 M_\oplus$ , respectively. We note that the injection–recovery

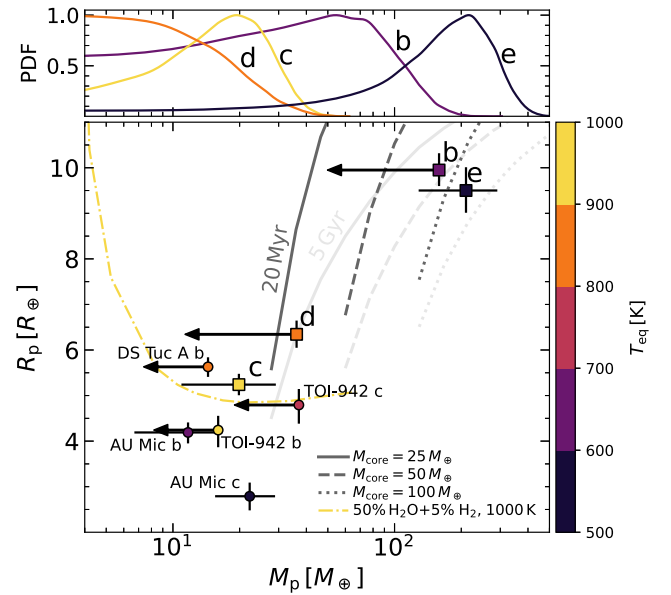
tests that were carried out (Appendix A.1 of the Appendix) suggest that our model systematically underestimates the mass of planet d by 10%–15%, which, when taken into account, increases planet d’s upper mass limit to  $M_d < 41.4 M_\oplus$ .

The mass constraints derived here are lower than those reported by Suárez Mascareño et al. (2021). These authors obtain detections of planets b and e and derive masses of  $M_b = 203 \pm 60 M_\oplus$  and  $M_e = 1.16 \pm 0.30 M_{\text{Jup}}$ , respectively. They also find  $2\sigma$  upper limits for planets c and d of  $M_c < 76 M_\oplus$  and  $M_d < 99 M_\oplus$ , respectively. The differences between these values and those derived in our study can potentially be attributed to various factors like the inclusion of additional RV measurements, the inclusion of new TESS observations that provide a greater constraint on planet e’s orbital period, and the sensitivity of the results to the adopted stellar activity model. The GP-based approach used in our analysis and adopted by Suárez Mascareño et al. (2021) suggests that the accuracy with which the system’s planetary RV signals can be recovered is sensitive to the choice of covariance function. Similar to the analysis carried out by Benatti et al. (2021) for the young DS Tuc A system, we find that adopting the quasi-periodic kernel (Equation (4)) yielded a higher accuracy with fewer systematic biases compared to the SHO kernel (Equation (1)), as evaluated using injection–recovery tests.

Most of the analysis presented in this work was carried out assuming circular orbits. When allowing for noncircular orbits for the adopted  $n_e = 51$  solution, we obtained  $2\sigma$  upper limits on the eccentricities of planets b, d, and e of  $e_b < 0.13$ ,  $e_d < 0.14$ , and  $e_e < 0.32$ , respectively. We note that Arevalo et al. (2022) derive a similar upper limit for planet b’s eccentricity of  $< 0.17$  using dynamical stability constraints based on the masses reported by Suárez Mascareño et al. (2021). In the case of planet c, we obtained a high eccentricity of  $e_c = 0.44^{+0.10}_{-0.12}$  and a much higher mass of  $M_c = 39 \pm 11 M_\oplus$ . However, considering (1) planet c’s relatively small RV semiamplitude ( $K_c = 5.7 \pm 2.6 \text{ m s}^{-1}$  assuming circular orbits), (2) the typical RV measurement uncertainty ( $\approx 10 \text{ m s}^{-1}$ ), and (3) the fact that sparse, low signal-to-noise ratio RV data sets are easily biased toward higher eccentricities (Shen & Turner 2008), we conclude that the high  $e_c$  and high  $M_c$  solution is likely biased and therefore not reliable.

### 5.1. Interior Structure and Evolution

In Figure 10, we compare our updated mass constraints and precise radii for V1298 Tau’s four transiting planets—derived for the  $n_e = 51$  ( $P_e = 46.768131 \pm 0.000076$  days) solution assuming circular orbits—with theoretical mass–radius relationships published by Fortney et al. (2007). We plot models calculated for an age of 20 Myr (black lines) and 5 Gyr (gray lines). The models consist of a core with a 50/50 mixture of ice and rock that is enshrouded by an H/He envelope; they include the effects of irradiation from a Sun-like host star at a distance of 0.1 au (V1298 Tau b, c, d, and e have semimajor axes ranging from 0.08 to 0.26 au). We find that planet e’s mass and radius are in good agreement with the  $100 M_\oplus$  core model. Based on the derived  $2\sigma$  upper mass limits, planet b is approximately consistent with the models calculated for core masses of 25– $100 M_\oplus$  while planet d is consistent with the  $25 M_\oplus$  core model. Planet c’s radius falls below the computed 20 Myr old evolutionary tracks, however, it is in close agreement with the model published by Zeng et al. (2019) that consists of a rocky core with an outer  $\text{H}_2\text{O}$  layer



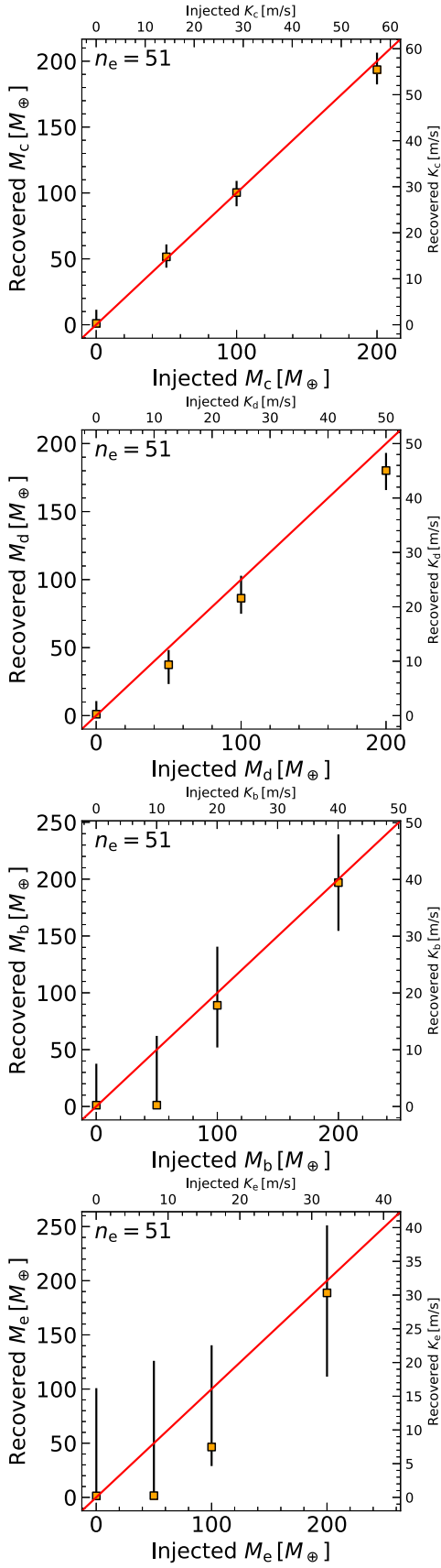
**Figure 10.** Masses and radii of V1298 Tau’s four transiting planets derived for the most probable  $P_e$  and assuming circular orbits (squares; upper mass limits correspond to  $2\sigma$ ) where the colors correspond to the equilibrium temperature. Five planets with mass constraints from three other young systems ( $< 100$  Myr) are plotted for comparison (circles): DS Tuc A b (Benatti et al. 2021), AU Mic b and c (Gilbert et al. 2022; Zicher et al. 2022), and TOI-942 b and c (Carleo et al. 2021). The dark-gray and light-gray lines are the theoretical planet mass–radius relations published by Fortney et al. (2007) at an age of 20 Myr and 5 Gyr, respectively. These models are computed for 50/50 ice-rock cores with H/He envelopes that are irradiated by a Sun-like host star at a distance of 0.1 au. The dashed–dotted curve is a model published by Zeng et al. (2019) composed of an Earth-like rocky core (47.5% by mass) with an  $\text{H}_2\text{O}$  layer (47.5%) and an  $\text{H}_2$  envelope (5%) at  $T_{\text{eq}} = 1000$  K.

(50/50 by mass) at an equilibrium temperature of 1000 K (see planet c’s  $T_{\text{eq}} = 979$  K).

Owen (2020) demonstrates how precise mass measurements of young, gas-rich planets orbiting close to their host stars such as V1298 Tau c can be used to test whether its formation is consistent with the core accretion theory or if the planet has gone through a rapid mass-loss “boil-off” phase. The derived mass of  $19.8^{+9.3}_{-8.9} M_\oplus$  and the conservative  $2\sigma$  upper limit of  $< 39 M_\oplus$  are both consistent with core accretion and do not require the invocation of boil-off to be explained. However, considering the low  $\approx 2\sigma$  significance of planet c’s recovered RV signature, additional RV measurements and/or TTV measurements are needed to confirm the derived  $M_c$  and further reduce the uncertainties.

### 5.2. Implications for Mass Loss

Based on X-ray observations of V1298 Tau, Poppenhaeger et al. (2020) conclude that, depending on the assumed stellar activity and planet masses, V1298 Tau’s inner three planets may currently have a relatively high atmospheric mass-loss rate such that their primordial H/He envelopes are eventually stripped away entirely. Maggio et al. (2022) predict that planets c and d are undergoing significant atmospheric evaporation if their masses are  $\lesssim 40 M_\oplus$  and  $\lesssim 33 M_\oplus$ , respectively. Planet c’s estimated mass of  $\approx 20 M_\oplus$  is therefore indicative of strong mass loss currently taking place while planet d’s  $2\sigma$  upper mass limit of  $M_d < 36 M_\oplus$  ( $M_d < 41.4 M_\oplus$  when accounting for the 15% bias noted above) is uninformative in terms of whether the planet is undergoing mass loss. Whether evaporation is



**Figure 11.** Injected vs. recovered planetary RV signatures. Note the differing axis scales.

occurring may be tested by searching for excess in-transit H/He absorption (e.g., Oklopčić & Hirata 2018; Allart et al. 2019; Feinstein et al. 2021; Vissapragada et al. 2021). Coupled with improved mass constraints (and better period constraints for planet e), such detections would help constrain atmospheric mass-loss models (e.g., Salz et al. 2016; Linssen et al. 2022).

### 5.3. Future RV Work

Additional high-precision RV measurements may be able to improve the mass constraints derived in this work further. We estimated how the results derived here could be improved if an additional 120 nightly RV measurements with uncertainties of  $10 \text{ m s}^{-1}$  are included in the analysis. The simulated measurements were generated using the general injection testing framework described in Appendix A.1 of the Appendix. The stellar activity was estimated from the HARPS-N GP activity model calculated using the median solution listed in Table 1 and shifted to the time stamps of the simulated measurements, which were arbitrarily set to start shortly after the last MAROON-X measurement. We assumed circular orbits and planet masses of  $M_b = 60 M_\oplus$ ,  $M_c = 20 M_\oplus$ ,  $M_d = 20 M_\oplus$ , and  $M_e = 200 M_\oplus$ . White noise defined by the measurement uncertainties and a  $5 \text{ m s}^{-1}$  instrumental jitter was then added to each simulated RV measurement and the NUTS sampling analysis was used to estimate the resulting uncertainties. We find that including the additional simulated RV measurements yields high-significance RV detections of planets b, c, and e with mass uncertainties of  $\approx 5\text{--}30 M_\oplus$ .

The mass constraints derived in our analysis have relatively large uncertainties primarily due to the impact of stellar activity: we find that applying our model to a simulated data set that includes only white noise due to measurement uncertainties and instrumental jitter yields mass uncertainties that are  $\lesssim 10 M_\oplus$  for all four planets. The systematic bias that causes planet d’s mass to be underestimated by  $\approx 10\%\text{--}15\%$  can also be attributed to imperfect modeling of the stellar activity. Therefore, in addition to obtaining more RV measurements, the derived mass constraints can likely be improved by adopting more physically motivated GP models (e.g., Luger et al. 2021), incorporating additional stellar activity tracers using 2D GPs (e.g., Barragán et al. 2021; Klein et al. 2021), and/or accounting for correlations with wavelength (Cale et al. 2021).

We thank John Livingston, Trevor David, and Erik Petigura for useful discussions that helped to guide and improve the work presented here. We also thank the anonymous referee for their critiques and helpful suggestions. The University of Chicago group acknowledges funding for the MAROON-X project from the David and Lucile Packard Foundation, the Heising-Simons Foundation, the Gordon and Betty Moore Foundation, the Gemini Observatory, the NSF (award number 2108465), and NASA (grant No. 80NSSC22K0117). The MAROON-X observations were collected under program GN-2021B-Q-103. A.D.F. acknowledges support by the National Science Foundation Graduate Research Fellowship Program under grant No. (DGE-1746045). This work was enabled by observations made from the Gemini-North telescope, located

within the Maunakea Science Reserve and adjacent to the summit of Maunakea. We are grateful for the privilege of observing the universe from a place that is unique in both its astronomical quality and its cultural significance.

*Facilities:* Gemini-North (MAROON-X), TESS (Ricker et al. 2014), and K2 (Borucki et al. 2010; Howell et al. 2014).

The TESS data presented in this paper were obtained from the Mikulski Archive for Space Telescopes (MAST) at the Space Telescope Science Institute. The specific observations analyzed can be accessed via [10.17909/72nn-2166](https://doi.org/10.17909/72nn-2166).

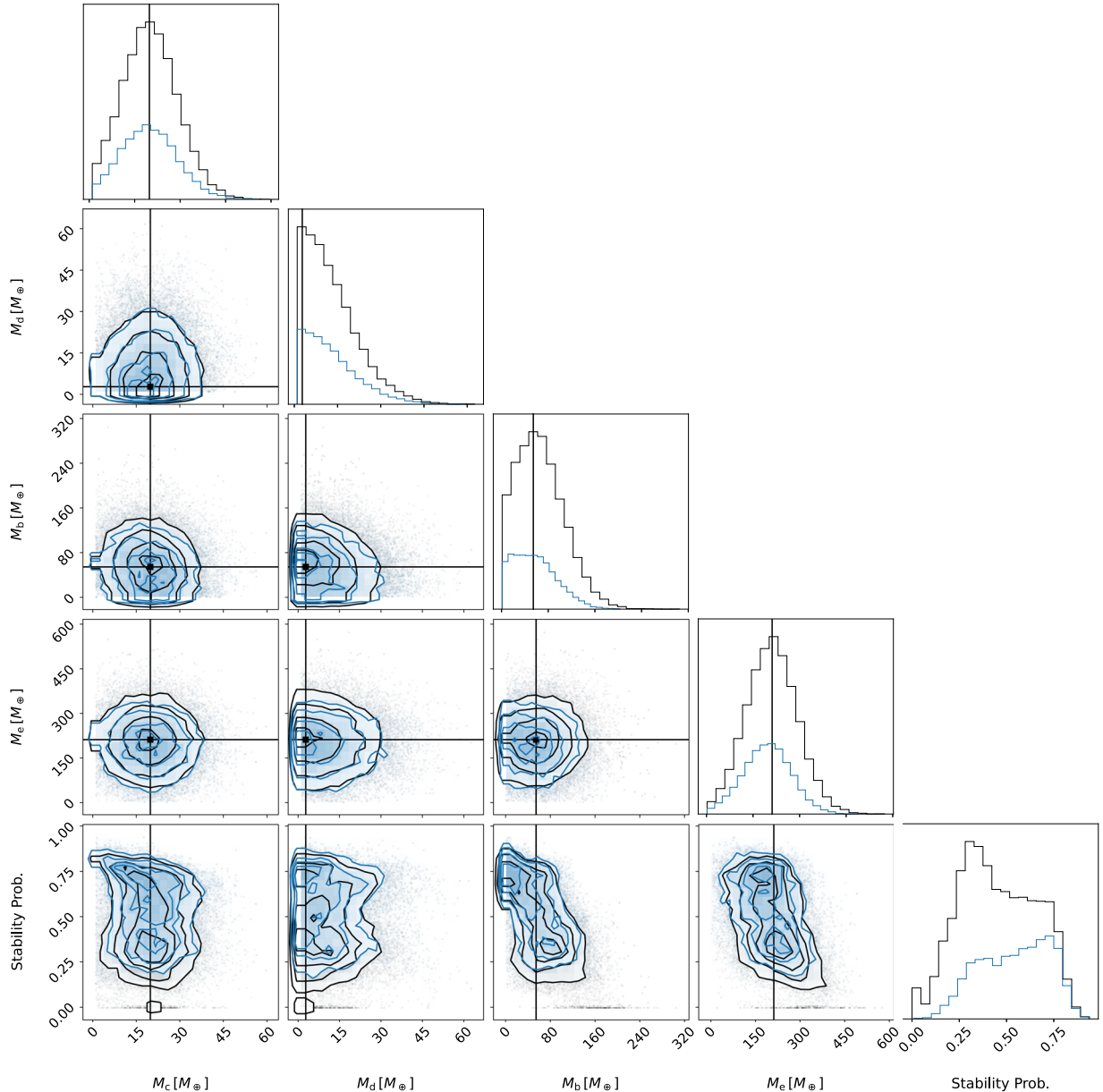
*Software:* AstroPy (Astropy Collaboration et al. 2013, 2018, 2022), celerite2 (Foreman-Mackey et al. 2017; Foreman-Mackey 2018), exoplanet (Foreman-Mackey et al. 2021), matplotlib (Hunter 2007), numpy (Harris et al. 2020), pymc3 (Salvatier et al. 2016), RadVel (Fulton et al. 2018), scipy (Virtanen et al. 2020), SERVAL (Zechmeister et al. 2018), and starry (Luger et al. 2019).

## Appendix

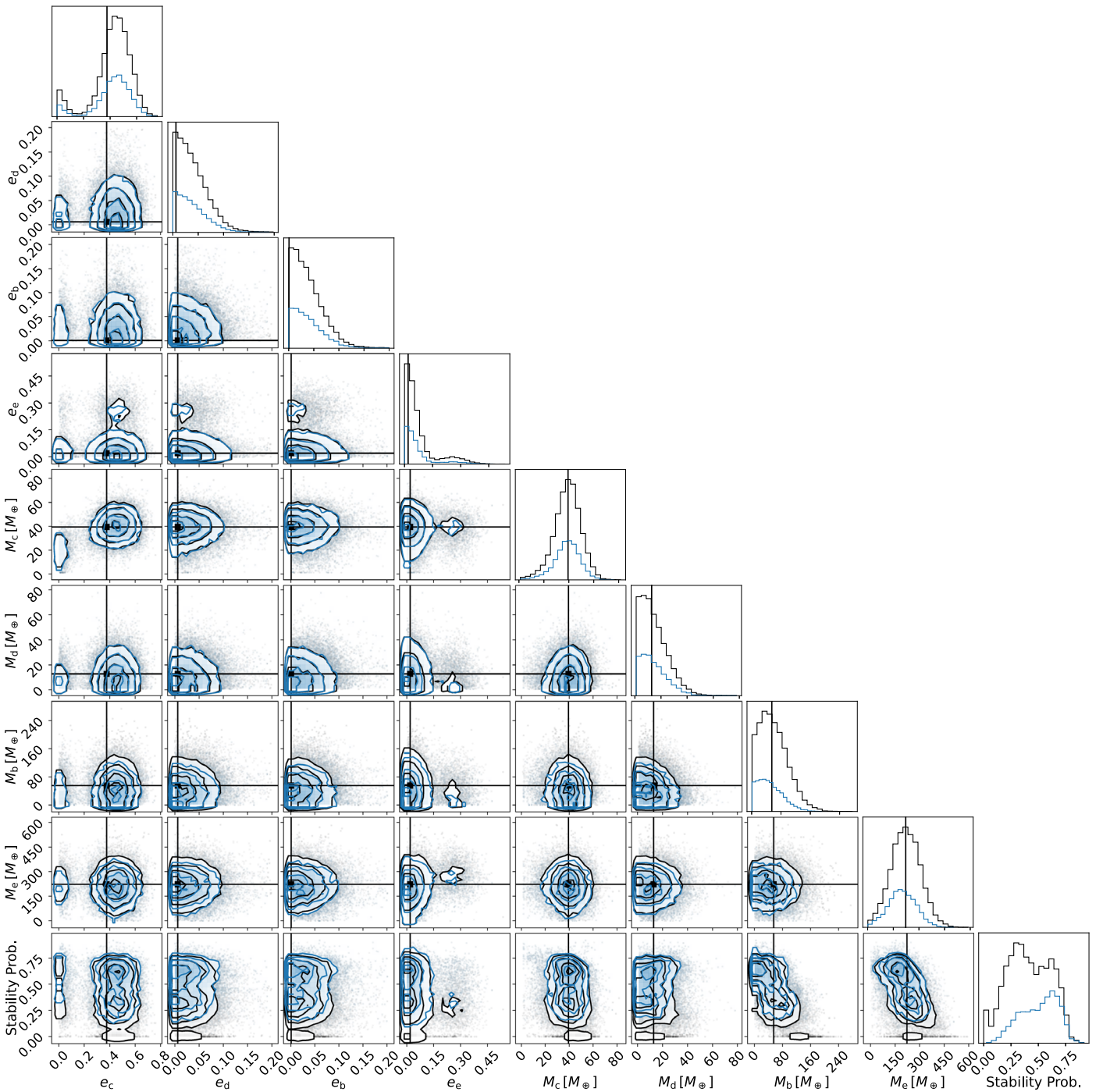
The derived transit times and  $O - C$  values are listed in Table 2. In Figure 12 we show the planetary mass posterior distributions for the adopted  $n_c = 51$  solution; a similar plot showing the mass and eccentricity posteriors for the non-circular case are shown in Figure 13.

### A.1. Injection Tests

Injection–recovery tests for the planetary RV signals were carried by modeling simulated RV measurements that include the planetary signals and the large stellar activity signals. For the stellar activity, we used the GP models associated with the median solution listed in Table 1 and shown in Figure 7, which do not include the planetary signals. Simulated planetary RV signals were generated assuming circular orbits for a grid of planet masses where each of the four planets was given a mass



**Figure 12.** Marginalized planet mass posteriors derived for the most probable  $n_c = 51$  solution assuming circular orbits (black contours). The dynamical stability probability ( $P(\text{Stable})$ ) estimated for each sample using SPOCK is also shown. The blue contours show the posteriors obtained after applying rejection sampling to the calculated  $P(\text{Stable})$  values.



**Figure 13.** Same as Figure 12 but for noncircular orbits where the eccentricity distributions are also plotted.

of  $0 M_{\oplus}$  (i.e., no signal),  $50 M_{\oplus}$ ,  $100 M_{\oplus}$ , or  $200 M_{\oplus}$ . The  $200 M_{\oplus}$  signals associated with the planets correspond to semiamplitudes of  $\approx 40\text{--}60 \text{ m s}^{-1}$ . We then injected the simulated planet-induced RVs into the activity model individually (i.e., for these tests, only a single planet’s RV signal is injected at a time) and added white noise with a variance defined by the measurement uncertainties and the median instrumental jitter hyperparameters ( $\sigma_i^2 + \sigma_{\text{jitter}}^2$ ). The NUTS sampling analysis was then applied to the simulated RV data sets along with the observed photometry in order to estimate the mass and uncertainties associated with the injected signal.

The results of the injection–recovery tests are shown in Figure 11. We find that planet c exhibits the highest accuracy and the smallest uncertainties with all injected signals being recovered within  $0.5\sigma$ . Planets b and e have significantly larger uncertainties and show that injected signals with  $M_b \lesssim 50 M_{\oplus}$  ( $K_b \lesssim 10 \text{ m s}^{-1}$ ) and  $M_e \lesssim 100 M_{\oplus}$  ( $K_e \lesssim 15 \text{ m s}^{-1}$ ) are not detected; the recovered masses all agree with the injected values with  $0.5\sigma$ . For planet d, a systematic bias is apparent in which the recovered masses are  $\approx 10\%$ – $15\%$  lower than the masses of the injected signals (corresponding to a difference in the semiamplitude of  $\approx 3\text{--}5 \text{ m s}^{-1}$ ). In this case, the recovered

$M_d$  for injected masses of 50–200  $M_\oplus$  are in agreement within  $1.5\sigma$ .

### ORCID iDs

James Sikora  <https://orcid.org/0000-0002-3522-5846>  
 Jason Rowe  <https://orcid.org/0000-0002-5904-1865>  
 Jacob L. Bean  <https://orcid.org/0000-0003-4733-6532>  
 Madison Brady  <https://orcid.org/0000-0003-2404-2427>  
 Jean-Michel Désert  <https://orcid.org/0000-0002-0875-8401>  
 Adina D. Feinstein  <https://orcid.org/0000-0002-9464-8101>  
 Emily A. Gilbert  <https://orcid.org/0000-0002-0388-8004>  
 Gregory Henry  <https://orcid.org/0000-0003-4155-8513>  
 David Kasper  <https://orcid.org/0000-0003-0534-6388>  
 Michael R. B. Matesic  <https://orcid.org/0000-0002-1119-7473>  
 Vatsal Panwar  <https://orcid.org/0000-0002-2513-4465>  
 Andreas Seifahrt  <https://orcid.org/0000-0003-4526-3747>  
 Hinna Shivkumar  <https://orcid.org/0000-0001-9289-0570>  
 Gudmundur Stefánsson  <https://orcid.org/0000-0001-7409-5688>  
 Julian Stürmer  <https://orcid.org/0000-0002-4410-4712>

### References

- Allart, R., Bourrier, V., Lovis, C., et al. 2019, *A&A*, **623**, A58  
 Arevalo, R. T., Tamayo, D., & Cranmer, M. 2022, *ApJL*, **932**, L12  
 Astropy Collaboration, Price-Whelan, A. M., Lim, P. L., et al. 2022, *ApJ*, **935**, 167  
 Astropy Collaboration, Price-Whelan, A. M., Sipőcz, B. M., et al. 2018, *AJ*, **156**, 123  
 Astropy Collaboration, Robitaille, T. P., Tollerud, E. J., et al. 2013, *A&A*, **558**, A33  
 Baraffe, I., Chabrier, G., & Barman, T. 2008, *A&A*, **482**, 315  
 Barragán, O., Aigrain, S., Rajpaul, V. M., & Zicher, N. 2021, *MNRAS*, **509**, 866  
 Benatti, S., Damasso, M., Borsari, F., et al. 2021, *A&A*, **650**, A66  
 Benatti, S., Nardiello, D., Malavolta, L., et al. 2019, *A&A*, **630**, A81  
 Berger, T. A., Huber, D., Gaidos, E., van Saders, J. L., & Weiss, L. M. 2020, *AJ*, **160**, 108  
 Borucki, W. J., Koch, D., Basri, G., et al. 2010, *Sci*, **327**, 977  
 Cale, B. L., Reece, M., Plavchan, P., et al. 2021, *AJ*, **162**, 295  
 Carleo, I., Desidera, S., Nardiello, D., et al. 2021, *A&A*, **645**, A71  
 Cloutier, R., Astudillo-Defru, N., Bonfils, X., et al. 2019, *A&A*, **629**, A111  
 David, T. J., Cody, A. M., Hedges, C. L., et al. 2019a, *AJ*, **158**, 79  
 David, T. J., Petigura, E. A., Luger, R., et al. 2019b, *ApJL*, **885**, L12  
 Feinstein, A. D., David, T. J., Montet, B. T., et al. 2022, *ApJL*, **925**, L2  
 Feinstein, A. D., Montet, B. T., Johnson, M. C., et al. 2021, *AJ*, **162**, 213  
 Foreman-Mackey, D. 2018, *RNAAS*, **2**, 31  
 Foreman-Mackey, D., Agol, E., Ambikasaran, S., & Angus, R. 2017, *AJ*, **154**, 220  
 Foreman-Mackey, D., Luger, R., Agol, E., et al. 2021, *JOSS*, **6**, 3285  
 Fortney, J. J., Marley, M. S., & Barnes, J. W. 2007, *ApJ*, **659**, 1661  
 Fulton, B. J., Petigura, E. A., Blunt, S., & Sinukoff, E. 2018, *PASP*, **130**, 044504  
 Gelman, A., & Rubin, D. B. 1992, *StaSc*, **7**, 457  
 Gilbert, E. A., Barclay, T., Quintana, E. V., et al. 2022, *AJ*, **163**, 147  
 Harris, C. R., Millman, K. J., van der Walt, S. J., et al. 2020, *Natur*, **585**, 357  
 Hoffman, M. D., & Gelman, A. 2014, arXiv:1111.4246  
 Howell, S. B., Sobek, C., Haas, M., et al. 2014, *PASP*, **126**, 398  
 Hunter, J. D. 2007, *CSE*, **9**, 90  
 Ibañez Bustos, R. V., Buccino, A. P., Flores, M., et al. 2019, *MNRAS*, **483**, 1159  
 Jenkins, J. M., Twicken, J. D., McCauliff, S., et al. 2016, *Proc. SPIE*, **9913**, 99133E  
 Kipping, D. M. 2013, *MNRAS*, **435**, 2152  
 Klein, B., Donati, J.-F., Moutou, C., et al. 2021, *MNRAS*, **502**, 188  
 Kulow, J. R., France, K., Linsky, J., & Parke Loyd, R. O. 2014, *ApJ*, **786**, 132  
 Lee, E. J., & Chiang, E. 2015, *ApJ*, **811**, 41  
 Lee, E. J., & Chiang, E. 2016, *ApJ*, **817**, 90  
 Linssen, D., Oklopčić, A., & MacLeod, M. 2022, *A&A*, **667**, A54  
 Lopez, E. D., & Fortney, J. J. 2014, *ApJ*, **792**, 1  
 Luger, R., Agol, E., Foreman-Mackey, D., et al. 2019, *AJ*, **157**, 64  
 Luger, R., Foreman-Mackey, D., & Hedges, C. 2021, *AJ*, **162**, 124  
 Luger, R., Kruse, E., Foreman-Mackey, D., Agol, E., & Saunders, N. 2018, *AJ*, **156**, 99  
 Maggio, A., Locci, D., Pillitteri, I., et al. 2022, *ApJ*, **925**, 172  
 Newton, E. R., Mann, A. W., Tofflemire, B. M., et al. 2019, *ApJL*, **880**, L17  
 Oklopčić, A., & Hirata, C. M. 2018, *ApJL*, **855**, L11  
 Owen, J. E. 2020, *MNRAS*, **498**, 5030  
 Plavchan, P., Barclay, T., Gagné, J., et al. 2020, *Natur*, **582**, 497  
 Poppenhaeger, K., Ketzler, L., & Mallonn, M. 2020, *MNRAS*, **500**, 4560  
 Ricker, G. R., Winn, J. N., Vanderspek, R., et al. 2014, *JATIS*, **1**, 014003  
 Rizzuto, A. C., Newton, E. R., Mann, A. W., et al. 2020, *AJ*, **160**, 33  
 Roberts, S., Osborne, M., Ebdon, M., et al. 2013, *RSPTA*, **371**, 20110550  
 Salvatier, J., Wiecki, T. V., & Fonnesbeck, C. 2016, *PeerJ Comp. Sci.*, **2**, e55  
 Salz, M., Schneider, P. C., Czesla, S., & Schmitt, J. H. M. M. 2016, *A&A*, **585**, L2  
 Seifahrt, A., Bean, J. L., Kasper, D., et al. 2022, *Proc. SPIE*, **12184**, 121841G  
 Seifahrt, A., Bean, J. L., Stürmer, J., et al. 2020, *Proc. SPIE*, **11447**, 114471F  
 Seifahrt, A., Stürmer, J., Bean, J. L., & Schwab, C. 2018, *Proc. SPIE*, **10702**, 107026D  
 Shen, Y., & Turner, E. L. 2008, *ApJ*, **685**, 553  
 Suárez Mascareño, A., Damasso, M., Lodieu, N., et al. 2021, *NatAs*, **6**, 232  
 Tamayo, D., Cranmer, M., Hadden, S., et al. 2020, *PNAS*, **117**, 18194  
 Tamayo, D., Gilbertson, C., & Foreman-Mackey, D. 2021, *MNRAS*, **501**, 4798  
 Van Eylen, V., Albrecht, S., Huang, X., et al. 2019, *AJ*, **157**, 61  
 Virtanen, P., Gommers, R., Oliphant, T. E., et al. 2020, *NatMe*, **17**, 261  
 Vissapragada, S., Stefánsson, G., Greklek-McKeon, M., et al. 2021, *AJ*, **162**, 222  
 Zechmeister, M., Reiners, A., Amado, P. J., et al. 2018, *A&A*, **609**, A12  
 Zeng, L., Jacobsen, S. B., Sasselov, D. D., et al. 2019, *PNAS*, **116**, 9723  
 Zicher, N., Barragán, O., Klein, B., et al. 2022, *MNRAS*, **512**, 3060